Journal of Scientific Computing (2023) 96:26
https://doi.org/10.1007/s10915-023-02238-x

Multidimensional Generalized Riemann Problem Solver for Maxwell's Equations

Arijit Hazra[1] · **Dinshaw S. Balsara**[2] · **Praveen Chandrashekar**[3] · **Sudip K. Garain**[4]

Received: 16 November 2022 / Revised: 25 March 2023 / Accepted: 29 April 2023 /
Published online: 31 May 2023

Abstract
Approximate multidimensional Riemann solvers are essential building blocks in designing globally constraint-preserving finite volume time domain and discontinuous Galerkin time domain schemes for computational electrodynamics (CED). In those schemes, we can achieve high-order temporal accuracy with the help of Runge–Kutta or ADER time-stepping. This paper presents the design of a multidimensional approximate generalized Riemann problem (GRP) solver for the first time. The multidimensional Riemann solver accepts as its inputs the four states surrounding an edge on a structured mesh, and its output consists of a resolved state and its associated fluxes. In contrast, the multidimensional GRP solver accepts as its inputs the four states and their gradients in all directions; its output consists of the resolved state and its corresponding fluxes and the gradients of the resolved state. The gradients can then be used to extend the solution in time. As a result, we achieve second-order temporal accuracy in a single step. In this work, the formulation is optimized for linear hyperbolic systems with stiff, linear source terms because such a formulation will find maximal use in CED. Our formulation produces an overall constraint-preserving time-stepping strategy based on the GRP that is provably L-stable in the presence of stiff source terms. We present several stringent test problems, showing that the multidimensional GRP solver for CED meets its design accuracy and performs stably with optimal time steps. The test problems include

✉ Arijit Hazra
ahazra@iitpkd.ac.in; mailtohazra@gmail.com

Dinshaw S. Balsara
dbalsara@nd.edu

Praveen Chandrashekar
praveen@math.tifrbng.res.in

Sudip K. Garain
sgarain@iiserkol.ac.in

1 Department of Mechanical Engineering, Indian Institute of Technology, Palakkad, Kerala, India

2 Department of Physics, University of Notre Dame, Notre Dame, IN, USA

3 TIFR Center for Applicable Mathematics, Bangalore, India

4 Department of Physical Sciences, Indian Institute of Science Education and Research, Kolkata, Mohanpur, West Bengal, India

cases with high conductivity, showing that the beneficial L-stability is indeed realized in practical applications.

Keywords Conservation laws · Hyperbolic partial differential equations · Multidimensional Riemann problem · Maxwell's equations

Mathematics Subject Classification 78M12 · 65M08 · 35L65

1 Introduction

Computational electrodynamics (CED) which deals with the numerical solution of Maxwell's equations, plays a vital role in many problems in science and engineering. The finite-difference time-domain (FDTD) method [1–5] has been a mainstay of CED applications. The primary strength of FDTD stems from its use of a beneficial staggering of the electric and magnetic fields to ensure that the global constraints (inherent in Gauss's law and the absence of magnetic monopoles) are discretely represented on the computational mesh. FDTD is globally constraint-preserving. However, the primary weakness of standard FDTD stems from the fact that it is restricted to second-order accuracy, especially when electromagnetic radiation interacts with material media.

The differential form of Maxwell's equations has a dissipationless and dispersionless limit. As a result, it is beneficial for numerical schemes to be as dissipationless and dispersionless as possible. This has given rise to the discontinuous Galerkin time domain (DGTD) methods [6–13]. Such methods do not satisfy the constraints in a global sense; though some of them do satisfy the constraints locally within each element. Even so, since they are based on discontinuous Galerkin methods, their strong point is that they can reach high orders of accuracy. It is very desirable to retain good traits of the FDTD and DGTD schemes discussed above.

In an effort to design CED schemes that offer the best of both worlds—global constraint preservation from FDTD and higher order from DGTD—we have embarked on an effort to design such schemes. Therefore, finite volume time domain (FVTD) schemes that globally preserve constraints and also attain high order of accuracy were presented in [14–16]. DGTD schemes with those same favorable attributes were presented in [17–19]. The two central ingredients of those schemes are a high order constraint-preserving reconstruction of vector fields [14–16, 20–24] and multidimensional Riemann solvers [25–32] The constraint-preserving reconstruction provides spatially high order accuracy. The multidimensional Riemann solver folds in the essential physics that electromagnetic phenomena are mediated by wave propagation that invariably occurs in all directions. It also gives us a natural, physics-based approach for obtaining the electric and magnetic fields at the edges of the computational mesh.

Furthermore, Maxwell's equations have symplectic and multi-symplectic structures. Considering this, Leapfrog time integration has been the chosen strategy for standard FDTD as it is a form of symplectic integrator. However, it is well-known that FDTD results in high level of dispersion error [4]. As this numerical dispersion error accumulates over time, simulation of long-term behaviour and long-duration electromagnetic wave propagation with FDTD requires an extremely fine mesh, and finer mesh in conjunction with courant stability criteria results in prohibitively high computational time for such simulations with FDTD. There have been several efforts to reduce the dispersion error by modifying FDTD [33]. However, con-

sidering all the desirable features of higher order numerical methods for CED, such as higher order spatial and temporal accuracy, ability to handle complex geometry, low dispersion error, higher-order CED schemes generally tend to use low-storage five-stage fourth-order Explicit Runge–Kutta method (LSERK4) [8, 34–38], strongly stability-preserving Runge–Kutta (SSPRK) [18, 19, 39, 40] or ADER (Arbitrary DERivatives in space and time) [41–44] time-discretizations [16, 45].

To compare briefly the computational complexities of Runge–Kutta and ADER time integration schemes for CED, we first note that each stage in a Runge–Kutta time-discretization is only first order accurate in time. For higher-order constraint-preserving time evolution of CED with Runge–Kutta schemes is, therefore, obtained by the application of a multidimensional Riemann solver at the edges of the mesh in order to obtain the edge-collocated integrals of the electric and magnetic fields. Thus each stage of a Runge–Kutta time-discretization is relatively inexpensive, but the overall scheme can be more expensive because multiple stages are used. Since the CED equations can have stiff source terms, the inclusion of stiff source terms can also add to the cost of a Runge–Kutta time-discretization. The ADER update only requires a single stage ADER formulation within each zone to make an "in-the-small" evolution within each zone. Once this is available, constraint-preserving time evolution of CED can be obtained with volumetrically-based ADER schemes by invoking a multidimensional Riemann solver at the edges of the mesh. However, for volumetrically-based ADER schemes the space-time ADER construction within a zone can itself be quite expensive. The treatment of stiff source terms also adds to the cost of an ADER scheme.

The utility of a GRP approach stems from the fact that a GRP can utilize not just the input states, but also their gradients. Realize that those gradients are always available, and they can always be provided by the spatial reconstruction. The intricacy in designing a GRP solver consists of finding ways to take the gradients of the input states and using them to obtain gradients in the resolved state. Once the gradients in the resolved state are obtained, one can obtain at least a second order accurate update in one stage. While a few exact and approximate GRP solvers have been designed that go beyond second order accuracy [46–55], the majority of GRP solvers have been restricted to second order in time [56–62]. All the GRP constructions that we know of have been one-dimensional. Since multidimensional Riemann solvers have begun to play such an important role in CED, and also other fields, it is of great interest to obtain generalized Riemann problem versions of the same.

In globally-constraint preserving schemes for CED, we apply a multidimensional Riemann solver to the edges of the mesh. Such multidimensional Riemann solvers have been designed [25–28, 31, 32, 63]. However, as far as we know, this is the first effort to formulate a multidimensional generalized Riemann problem solver that works seamlessly. The goal of this first paper is to design a multidimensional generalized Riemann solver for CED. We choose CED because it is a linear hyperbolic system and it is very beneficial to study the problem in the context of a linear system before tackling the fully non-linear case. The fully non-linear case will be formulated in a subsequent paper. We formulate the problem so that it can be used for any general linear hyperbolic system, but we also specialize our results for CED.

CED, just like aeroacoustics, is very special in that most applications are linear. If non-linearities are present, they are usually mild. But that only changes the emphasis of the solution methodology. Because waves can propagate without dissipation or dispersion in electrodynamics and aeroacoustics, a substantial premium is placed on minimizing numerical dispersion and dissipation. There has been a growing realization that the availability of GRP solvers can lead to a new generation of low-dissipation, low-dispersion Taylor Series-based (TS-based) schemes [64–66], though that field is perhaps still emergent. The schemes are

referred to as Taylor series-based because the GRP solver delivers not just the numerical flux but also its derivative in time.

The novelty of our work lies in presenting a multidimensional GRP solver, which can be an essential building block for the development of low dissipation, low dispersion TS-based schemes for CED, aeroacoustics and other analogous fields. We also show how linear stiff source terms can be included in the multidimensional GRP solver.

The rest of the paper is organized as follows. In Sect. 2 we describe Maxwell's equations and globally constraint-preserving solution methods for those equations. The multidimensional GRP solver is described in Sect. 3. Section 4 gives a pointwise strategy for implementation. Section 5 provides accuracy analysis; Sect. 6 provides several stringent test problems. Section 7 draws some conclusions.

2 Maxwell Equation

We split this Section into two parts. Section 2.1 introduces Maxwell's equations. Section 2.2 describes their globally constraint-preserving numerical solution using a GRP solver.

2.1 Introduction to Maxwell's Equations

The equations of CED can be written as two evolutionary curl-type equations for the magnetic induction and the electric displacement. The first of these is Faraday's law, given by,

$$\frac{\partial \boldsymbol{B}}{\partial t} + \nabla \times \boldsymbol{E} = -\boldsymbol{M}, \tag{2.1}$$

where $\boldsymbol{B}$ is the magnetic induction (or magnetic flux density), $\boldsymbol{E}$ is the electric field and $\boldsymbol{M}$ is the the magnetic current density. The magnetic current density is zero for any physical domain. The second evolutionary equation for the electric displacement is the extended Ampere's law, given by

$$\frac{\partial \boldsymbol{D}}{\partial t} - \nabla \times \boldsymbol{H} = -\boldsymbol{J}, \tag{2.2}$$

where $\boldsymbol{D}$ is the electric displacement (or electric flux density), $\boldsymbol{H}$ is the magnetic field vector and $\boldsymbol{J}$ is the electric current density. The structure of the above two equations is such that the magnetic induction and the electric displacement also satisfy the following two non-evolutionary involution constraints, given by

$$\nabla \cdot \boldsymbol{B} = \rho_M, \tag{2.3}$$

and

$$\nabla \cdot \boldsymbol{D} = \rho_E. \tag{2.4}$$

Here ρ_M and ρ_E are the magnetic and electric charge densities. For any physical medium $\rho_M = 0$ since magnetic monopoles do not exist.

The involutionary nature of the above equations ensures that the electric charge density satisfies the equation

$$\frac{\partial \rho_E}{\partial t} + \nabla \cdot \boldsymbol{J} = 0, \tag{2.5}$$

and the magnetic charge density satisfies the equation

$$\frac{\partial \rho_M}{\partial t} + \nabla \cdot \boldsymbol{M} = 0. \tag{2.6}$$

In material media we also have the constitutive relations

$$\boldsymbol{B} = \mu \boldsymbol{H}, \tag{2.7}$$

and

$$\boldsymbol{D} = \varepsilon \boldsymbol{E}, \tag{2.8}$$

where μ is a 3×3 permeability tensor and ε is the analogous 3×3 permittivity tensor. For most material media, these tensors are diagonal. The eigenstructure of the hyperbolic system is most easily found for the diagonal case, where we make the simplifying assumption $\varepsilon = \text{diag}\{\varepsilon_{xx}, \varepsilon_{yy}, \varepsilon_{zz}\}$ and $\mu = \text{diag}\{\mu_{xx}, \mu_{yy}, \mu_{zz}\}$. The corresponding eigenstructure has been catalogued in Sub-section II.2 of [15]. We will also need the inverses of the permittivity and permeability tensors. These 3×3 inverse matrices will also be symmetric, and we denote them as $\tilde{\boldsymbol{\varepsilon}}$ and $\tilde{\boldsymbol{\mu}}$.

The current density is related to the electric field via

$$\boldsymbol{J} = \sigma \boldsymbol{E}, \tag{2.9}$$

where σ is the conductivity. Similarly, the magnetic current density is related to the magnetic field via

$$\boldsymbol{M} = \sigma^* \boldsymbol{H}, \tag{2.10}$$

where is the equivalent magnetic loss, which is again zero in physical media, but may be non-zero when imposing boundary conditions in CED.

2.2 Globally Constraint-Preserving Numerical Solution of Maxwell's Equations

The facially-collocated normal components of the electric displacement and the magnetic induction constitute the primal variables of our scheme In Fig. 1, these vector fields are shown by the thick red arrow and the thick blue arrow, respectively, in each of the faces of the cuboidal element. In a finite-volume sense, these primal variables are actually taken to be facial averages of the normal components of the electric displacement and the magnetic induction. The overall task consists of finding the edge-collocated components of the magnetic field vector and the electric field vector, shown in Fig. 1. These are shown with the thinner red arrow and the thinner blue arrow, respectively, next to the edges of the zone shown in Fig. 1. In a finite-volume sense, these are actually averages in one space dimension (taken to be the length of the element's edge) and the time dimension (evaluated over the timestep). The order of spatial reconstruction of the electric displacement and the magnetic induction then determines the order of spatial accuracy of our numerical scheme. At second order, volumetric ADER schemes of the sort designed in [41, 43] can indeed provide a one-step update. However, a similar one-step update can be obtained using the multidimensional GRP solver designed here.

A single step constraint-preserving update for the entire set of CED equations, consistent with the curl-type update in Eqs. (2.1) and (2.2) can be written at each face of the zone shown in Fig. 1 as

$$\bar{D}^{n+1}_{x;i+\frac{1}{2},j,k} = \bar{D}^{n}_{x;i+\frac{1}{2},j,k} - \Delta t \, \bar{J}^{n+\frac{1}{2}}_{x;i+\frac{1}{2},j,k} + \frac{\Delta t}{\Delta y \Delta z}$$

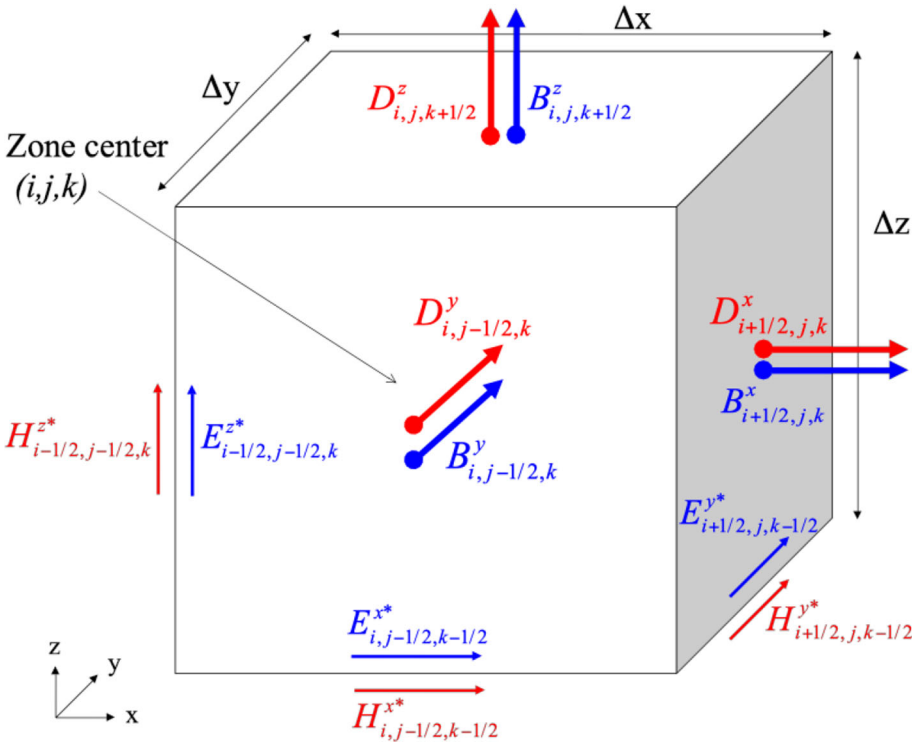

Fig. 1 Schematic diagram depicting the collocation of the primal and dual variables of Maxwell's equations. Primal variables of the scheme, given by the normal components of the magnetic induction and electric field displacement, are facially-collocated. They undergo an update from Faraday's law and the generalized Ampere's law, respectively. The components of the primal magnetic induction vector are shown by the thick blue arrows, while the components of the primal electric displacement vector are shown by the thick red arrows. The edge-collocated electric fields, which are used for updating the facial magnetic induction components, are shown by the thin blue arrows close to the appropriate edge. The edge-collocated magnetic fields, which are used for updating the facial electric displacement components, are shown by the thin red arrows close to the appropriate edge (Color figure online)

$$\left(\Delta z\ \bar{H}^{n+\frac{1}{2}}_{z;\,i+\frac{1}{2},j+\frac{1}{2},k} - \Delta z\ \bar{H}^{n+\frac{1}{2}}_{z;\,i+\frac{1}{2},j-\frac{1}{2},k} + \Delta y\ \bar{H}^{n+\frac{1}{2}}_{y;i+\frac{1}{2},j,k-\frac{1}{2}} - \Delta y\ \bar{H}^{n+\frac{1}{2}}_{y;i+\frac{1}{2},j,k+\frac{1}{2}}\right) \tag{2.11a}$$

$$\bar{D}^{n+1}_{y;i,j-\frac{1}{2},k} = \bar{D}^{n}_{y;i,j-\frac{1}{2},k} - \Delta t\ \bar{J}^{n+\frac{1}{2}}_{y;i,j-\frac{1}{2},,k} + \frac{\Delta t}{\Delta z \Delta x}\left(\Delta x\ \bar{H}^{n+\frac{1}{2}}_{x;\,i,j-\frac{1}{2},k+\frac{1}{2},} - \Delta x\ \bar{H}^{n+\frac{1}{2}}_{x;i,j-\frac{1}{2},k-\frac{1}{2},} + \Delta z\ \bar{H}^{n+\frac{1}{2}}_{z;i-\frac{1}{2},j-\frac{1}{2},k} - \Delta z\ \bar{H}^{n+\frac{1}{2}}_{z;i+\frac{1}{2},j-\frac{1}{2},k}\right) \tag{2.11b}$$

$$\bar{D}^{n+1}_{z;i,j,k+\frac{1}{2}} = \bar{D}^{n}_{z;i,j,k+\frac{1}{2}} - \Delta t\ \bar{J}^{n+\frac{1}{2}}_{z;i,j,k+\frac{1}{2}} + \frac{\Delta t}{\Delta x \Delta y}\left(\Delta x\ \bar{H}^{n+\frac{1}{2}}_{x;\,i,j-\frac{1}{2},k+\frac{1}{2}} - \Delta x\ \bar{H}^{n+\frac{1}{2}}_{x;i,j+\frac{1}{2},k+\frac{1}{2}} + \Delta y\ \bar{H}^{n+\frac{1}{2}}_{y;i+\frac{1}{2},j,k+\frac{1}{2}} - \Delta y\ \bar{H}^{n+\frac{1}{2}}_{y;i-\frac{1}{2},j,k+\frac{1}{2}}\right) \tag{2.11c}$$

$$\bar{B}^{n+1}_{x;i+\frac{1}{2},j,k} = \bar{B}^{n}_{x;i+\frac{1}{2},j,k} - \Delta t\, \bar{M}^{n+\frac{1}{2}}_{x;i+\frac{1}{2},j,k} - \frac{\Delta t}{\Delta y \Delta z}\left(\Delta z\, \bar{E}^{n+\frac{1}{2}}_{z;\, i+\frac{1}{2},j+\frac{1}{2},k} - \Delta z\, \bar{E}^{n+\frac{1}{2}}_{z;\, i+\frac{1}{2},j-\frac{1}{2},k} + \Delta y\, \bar{E}^{n+\frac{1}{2}}_{y;i+\frac{1}{2},j,k-\frac{1}{2}} - \Delta y\, \bar{E}^{n+\frac{1}{2}}_{y;i+\frac{1}{2},j,k+\frac{1}{2}}\right) \tag{2.11d}$$

$$\bar{B}^{n+1}_{y;i,j-\frac{1}{2},k} = \bar{B}^{n}_{y;i,j-\frac{1}{2},k} - \Delta t\, \bar{M}^{n+\frac{1}{2}}_{y;i,j-\frac{1}{2},,k} - \frac{\Delta t}{\Delta z \Delta x}\left(\Delta x\, \bar{E}^{n+\frac{1}{2}}_{x;\, i,j-\frac{1}{2},k+\frac{1}{2},} - \Delta x\, \bar{E}^{n+\frac{1}{2}}_{x;i,j-\frac{1}{2},k-\frac{1}{2},} + \Delta z\, \bar{E}^{n+\frac{1}{2}}_{z;i-\frac{1}{2},j-\frac{1}{2},k} - \Delta z\, \bar{E}^{n+\frac{1}{2}}_{z;i+\frac{1}{2},j-\frac{1}{2},k}\right) \tag{2.11e}$$

$$\bar{B}^{n+1}_{z;i,j,k+\frac{1}{2}} = \bar{B}^{n}_{z;i,j,k+\frac{1}{2}} - \Delta t\, \bar{M}^{n+\frac{1}{2}}_{z;i,j,k+\frac{1}{2}} - \frac{\Delta t}{\Delta x \Delta y}\left(\Delta x\, \bar{E}^{n+\frac{1}{2}}_{x;\, i,j-\frac{1}{2},k+\frac{1}{2}} - \Delta x\, \bar{E}^{n+\frac{1}{2}}_{x;i,j+\frac{1}{2},k+\frac{1}{2}} + \Delta y\, \bar{E}^{n+\frac{1}{2}}_{y;i+\frac{1}{2},j,k+\frac{1}{2}} - \Delta y\, \bar{E}^{n+\frac{1}{2}}_{y;i-\frac{1}{2},j,k+\frac{1}{2}}\right). \tag{2.11f}$$

The reconstructed values for the electric displacement and magnetic induction, as well as their gradients, form the inputs to the multidimensional GRP. The multidimensional GRP is invoked at each edge. As an output, the GRP gives the time evolution of the resolved state that straddles the edge being considered. From this resolved state, we can evaluate the discrete curl of the electric and magnetic fields along each edge to obtain the globally constraint-preserving update in Eq. (2.11). We also have to pay attention, of course, to the source terms for the electric current density and the magnetic current density; these terms are usually stiff and should be handled with a scheme that is unconditionally stable. Furthermore, we want the asymptotic behaviour of the discrete update in Eq. (2.11) to be such that as $\Delta t \to \infty$ the discrete treatment of the source terms gives the same asymptotic result as the differential form of the PDE. Such an unconditional stability is also known as L-stability, and we discuss this in a later section.

3 Design of a Multidimensional GRP Solver for Maxwell's Equations and Linear Hyperbolic Partial Differential Equations in General

Maxwell's equations can be written as a system of PDE in the following manner

$$\frac{\partial \mathbf{U}}{\partial t} + \frac{\partial \boldsymbol{F}(\mathbf{U})}{\partial x} + \frac{\partial \boldsymbol{G}(\mathbf{U})}{\partial y} + \frac{\partial \boldsymbol{H}(\mathbf{U})}{\partial x} = \boldsymbol{S}(\mathbf{U}), \tag{3.1}$$

where

$$\mathbf{U} = \begin{pmatrix} D_x \\ D_y \\ D_z \\ B_x \\ B_y \\ B_z \end{pmatrix}, \quad \boldsymbol{F} = \begin{pmatrix} 0 \\ \tilde{\mu}_{xz}B_x + \tilde{\mu}_{yz}B_y + \tilde{\mu}_{zz}B_z \\ -\tilde{\mu}_{xy}B_x - \tilde{\mu}_{yy}B_y - \tilde{\mu}_{yz}B_z \\ 0 \\ -\tilde{\varepsilon}_{xz}D_x - \tilde{\varepsilon}_{yz}D_y - \tilde{\varepsilon}_{zz}D_z \\ \tilde{\varepsilon}_{xy}D_x + \tilde{\varepsilon}_{yy}D_y + \tilde{\varepsilon}_{yz}D_z \end{pmatrix}, \quad \boldsymbol{G} = \begin{pmatrix} -\tilde{\mu}_{xz}B_x - \tilde{\mu}_{yz}B_y - \tilde{\mu}_{zz}B_z \\ 0 \\ \tilde{\mu}_{xx}B_x + \tilde{\mu}_{xy}B_y + \tilde{\mu}_{xz}B_z \\ \tilde{\varepsilon}_{xz}D_x + \tilde{\varepsilon}_{yz}D_y + \tilde{\varepsilon}_{zz}D_z \\ 0 \\ -\tilde{\varepsilon}_{xx}D_x - \tilde{\varepsilon}_{xy}D_y - \tilde{\varepsilon}_{xz}D_z \end{pmatrix},$$

$$\boldsymbol{H} = \begin{pmatrix} \tilde{\mu}_{xy}B_x + \tilde{\mu}_{yy}B_y + \tilde{\mu}_{yz}B_z \\ -\tilde{\mu}_{xx}B_x - \tilde{\mu}_{xy}B_y - \tilde{\mu}_{xz}B_z \\ 0 \\ -\tilde{\varepsilon}_{xy}D_x - \tilde{\varepsilon}_{yy}D_y - \tilde{\varepsilon}_{yz}D_z \\ \tilde{\varepsilon}_{xx}D_x + \tilde{\varepsilon}_{xy}D_y + \tilde{\varepsilon}_{xz}D_z \\ 0 \end{pmatrix}, \quad \boldsymbol{S} = \begin{pmatrix} -\sigma(\tilde{\varepsilon}_{xx}D_x + \tilde{\varepsilon}_{xy}D_y + \tilde{\varepsilon}_{xz}D_z) \\ -\sigma(\tilde{\varepsilon}_{xy}D_x + \tilde{\varepsilon}_{yy}D_y + \tilde{\varepsilon}_{yz}D_z) \\ -\sigma(\tilde{\varepsilon}_{xz}D_x + \tilde{\varepsilon}_{yz}D_y + \tilde{\varepsilon}_{zz}D_z) \\ -\sigma^*(\tilde{\mu}_{xx}D_x + \tilde{\mu}_{xy}D_y + \tilde{\mu}_{xz}D_z) \\ -\sigma^*(\tilde{\mu}_{xy}D_x + \tilde{\mu}_{yy}D_y + \tilde{\mu}_{yz}D_z) \\ -\sigma^*(\tilde{\mu}_{xz}D_x + \tilde{\mu}_{yz}D_y + \tilde{\mu}_{zz}D_z) \end{pmatrix}.$$

In the above equations, $\tilde{\mu}_{ij}$ and $\tilde{\varepsilon}_{ij}$ represents different components of $\tilde{\boldsymbol{\mu}}$ and $\tilde{\boldsymbol{\varepsilon}}$ tensors where $\tilde{\boldsymbol{\mu}}$ and $\tilde{\boldsymbol{\varepsilon}}$ are inverses of 3×3 symmetric electric permittivity tensor $\boldsymbol{\varepsilon}$ and symmetric magnetic permeability tensor $\boldsymbol{\mu}$, respectively.

In light of the linearity of the fluxes and source terms in Maxwell's equations, the above equation can be written in terms of the Jacobians of the fluxes and the Jacobian of the source terms as follows

$$\frac{\partial \mathbf{U}}{\partial t} + \tilde{\boldsymbol{A}}\frac{\partial \mathbf{U}}{\partial x} + \tilde{\boldsymbol{B}}\frac{\partial \mathbf{U}}{\partial y} + \tilde{\boldsymbol{C}}\frac{\partial \mathbf{U}}{\partial z} = -\tilde{\boldsymbol{\Sigma}}\mathbf{U}. \tag{3.2}$$

In the above equation, $\tilde{\boldsymbol{A}}$, $\tilde{\boldsymbol{B}}$ and $\tilde{\boldsymbol{C}}$ are solution-independent characteristic matrices obtained from the x, y, z-fluxes. Likewise, $\tilde{\boldsymbol{\Sigma}} = -\frac{\partial \boldsymbol{S}(\mathbf{U})}{\partial \mathbf{U}}$ is a constant matrix, where the negative sign has been introduced just to respect the fact that the current terms in Maxwell's equations are written with a negative sign in front.

We would like to design a multidimensional approximate GRP solver for Eq. (3.2) specializing it to Maxwell's equations.

To describe the development of multidimensional GRP in a step-by-step manner, we split this section into several parts. In Sect. 3.1, we briefly describe the 1D Riemann problem (RP) and generalized Riemann problem (GRP) solvers. This provides us with the lead in to multidimensional Riemann solvers and the multidimensional GRP solver without any source term that we describe in Sect. 3.2. In Sect. 3.3, we show how this can be used to obtain a GRP without a source term. In Sect. 3.4, we show how the solution of the GRP is obtained in presence of a linear stiff source term.

3.1 One Dimensional Riemann Problem and Generalized Riemann Problem Solvers for Linear System

A one-dimensional Riemann solver operates at the faces of a mesh because that is where the one-dimensional discontinuities can be diagnosed on a mesh. It takes the two states at a face as input states and provides the resolved state and one-dimensional flux as output (Left panel of Fig. 2).

Analogously, a one-dimensional GRP solver also operates at the faces of a mesh. However, it takes the two states at a face, as well as their spatial gradients, as input states and provides the resolved state and one-dimensional flux and the gradient of the resolved state, as output (Right panel of Fig. 2). The output can then be used to extend the resolved state and its fluxes in time. Please note that we consider the approximate HLL Riemann solver here, which produces only one constant intermediate state between two interacting states. The expression for resolved state is given by [67]:

$$\mathbf{U}^* = -\frac{1}{S_R - S_L}\Big[(\tilde{\boldsymbol{A}} - S_R\mathbf{I})\mathbf{U}_R - (\tilde{\boldsymbol{A}} - S_L\mathbf{I})\mathbf{U}_L\Big], \quad \mathbf{I}: \text{Identity Matrix}, \tag{3.3}$$

where S_R and S_L are extremal speeds in right and left directions.

For a linear hyperbolic system, as S_R and S_L is constant, we can find the derivatives of the resolved state analytically with respect to any arbitrary r direction where r can be any

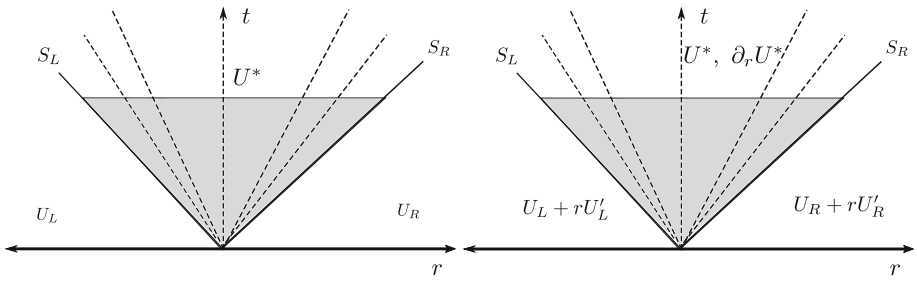

Fig. 2 One dimensional solvers that operate at the faces of a mesh. Left panel: One dimensional approximate Riemann solver. It takes two states U_L and U_R at the face as inputs and provides a single resolved state U^* as we use HLL Riemann solver here. Right panel: One dimensional Generalized Riemann solver for linear hyperbolic system. It takes left state U_L, right state U_R and their derivatives $\partial_r U_L$ and $\partial_r U_R$ as inputs where r represents any one of the $x,\ y,\ z$ direction in a Cartesian mesh and provides a resolved state U^* and the derivative $\partial_r U^*$ as outputs. As for linear hyperbolic systems (like Maxwell's equations) maximal wave speeds S_L, S_R are constant, the characteristics curves become straight lines even for GRP

one of $x,\ y$, or z in a Cartesian mesh, and it is given by,

$$\partial_r \mathbf{U}^* = -\frac{1}{S_R - S_L}\Big[(\tilde{\boldsymbol{A}} - S_R\mathbf{I})\ \partial_r \mathbf{U}_R - (\tilde{\boldsymbol{A}} - S_L\mathbf{I})\ \partial_r \mathbf{U}_L\Big]. \tag{3.4}$$

We use expressions (3.3) and (3.4) in the next section to obtain resolved states and their derivatives from one dimensional Riemann solvers that are required for a complete description of our multidimensional GRP-based scheme for linear hyperbolic systems.

3.2 Multidimensional Riemann Solver and Generalized Riemann Solver for Linear System

A multidimensional Riemann solver operates at the edges of a mesh because that is where the multidimensional discontinuities can be diagnosed on a mesh. We assume a Cartesian mesh to simplify the discussion, but the discussion is indeed generalizable. The multidimensional Riemann solver takes the four states that come together at an edge as input states and provides the resolved state (traditionally called a strongly-interacting state) and multidimensional fluxes as output. Analogously, the multidimensional GRP solver also operates at the edges of the mesh. However, the multidimensional GRP solver takes four states together with their spatial gradients as inputs. As outputs, it produces the strongly-interacting state and multidimensional fluxes, as well as the gradients of the strongly-interacting state. The output can then be used to extend the strongly-interacting state and its fluxes in time.

The edge-based arrangement of electric and magnetic fields for CED in Fig. 1 shows that the multidimensional GRP solver provides exactly the desired edge-based data at the very location this data is needed. This highlights the special utility of the multidimensional GRP solver for CED and other involution-constrained applications.

The GRP solver is two dimensional, because we would like to invoke it at the edges of the mesh. For illustration, we choose the GRP solver invoked at z-edge, and as a result, we focus on the xy-plane. However, we will retain derivatives with respect to all three axes in Eq. (3.2) as we realize that it might be beneficial to retain the variation in the third direction in fully three-dimensional CED problems.

For a structured mesh, the specification of the multidimensional Riemann problem at the edges of a Cartesian mesh requires the specification of four input states [25–27]. These input

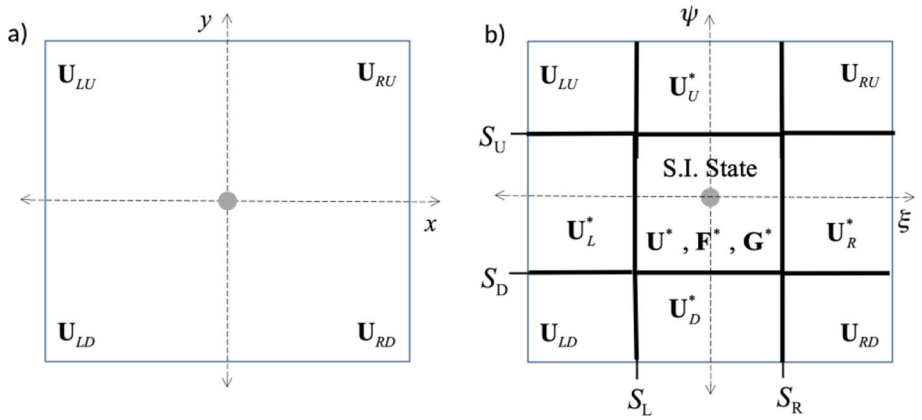

Fig. 3 **a** Four input states $\mathbf{U}_{LU}$, $\mathbf{U}_{RU}$, $\mathbf{U}_{LD}$, $\mathbf{U}_{RD}$ at the z-edge of a mesh, where one is looking down along the z-axis. **b** Strongly-interacting state from multidimensional Riemann problem and resolved states from the one-dimensional Riemann problems. While the left panel is in physical space, the right panel is best shown in terms of the wave speeds. Here, $\xi = x/t$ and $\psi = y/t$ are the wave speeds in the x- and y-directions

states at the initial time are called $\mathbf{U}_{RU}$ (for right-up), $\mathbf{U}_{LU}$ (for left-up), $\mathbf{U}_{LD}$ (for left-down) and $\mathbf{U}_{RD}$ (for right-down). Figure 3a shows the input states at the z-edge of a mesh, where one is looking down along the z-axis. As soon as those input states begin to interact, i.e. at a time that is later than the initial time, four one dimensional Riemann problems get established between the four states. Therefore, between the states $\mathbf{U}_{RU}$ and $\mathbf{U}_{LU}$ an x-directional Riemann problem gives rise to the resolved state $\mathbf{U}^*_U$; another x-directional Riemann problem between the states $\mathbf{U}_{RD}$ and $\mathbf{U}_{LD}$ gives rise to the resolved state $\mathbf{U}^*_D$; a y-directional Riemann problem between the states $\mathbf{U}_{RU}$ and $\mathbf{U}_{RD}$ gives rise to the resolved state $\mathbf{U}^*_R$; similarly a y-directional Riemann problem between the states $\mathbf{U}_{LU}$ and $\mathbf{U}_{RD}$ gives rise to the resolved state $\mathbf{U}^*_L$. Figure 3b shows how these resolved states from the one-dimensional Riemann problems are established. When these one-dimensional Riemann problems interact, they form another self-similarly evolving strongly-interacting state $\mathbf{U}^*$ which yields corresponding x and y fluxes $\boldsymbol{F}^*$ and $\boldsymbol{G}^*$. Figure 3b also shows this strongly-interacting state. While Figure 3a is in physical space, Fig. 3b is best shown in terms of the wave speeds. Please note that we use the approximate HLL Riemann solver which produces only one constant intermediate state between two interacting states. As a result, the four resolved states $\mathbf{U}^*_R$, $\mathbf{U}^*_L$, $\mathbf{U}^*_U$, $\mathbf{U}^*_D$ are constant states without sub-structure. Likewise, the state $\mathbf{U}^*$ has no sub-structure.

Because the characteristic matrices are constant, the extremal speeds in the x-direction span $\xi \in [S_L,\ S_R]$ and in the y-direction span $\psi \in [S_D,\ S_U]$ are also constant. S_R, S_L are extremal speeds associated with characteristic matrix $\tilde{\boldsymbol{A}}$ and S_U, S_D are extremal speeds associated with characteristic matrix $\tilde{\boldsymbol{B}}$. For the case of CED with diagonal permittivity and permeability, we have

$$\begin{aligned} S_R &= \max(\sqrt{\tilde{\mu}_{zz}\tilde{\varepsilon}_{xx}},\ \sqrt{\tilde{\mu}_{yy}\tilde{\varepsilon}_{zz}}), \quad S_L = -S_R, \\ S_U &= \max(\sqrt{\tilde{\mu}_{xx}\tilde{\varepsilon}_{zz}},\ \sqrt{\tilde{\mu}_{zz}\tilde{\varepsilon}_{xx}}), \quad S_D = -S_U. \end{aligned} \tag{3.5}$$

So we see that the extremal wave speeds are very easy to calculate for CED.

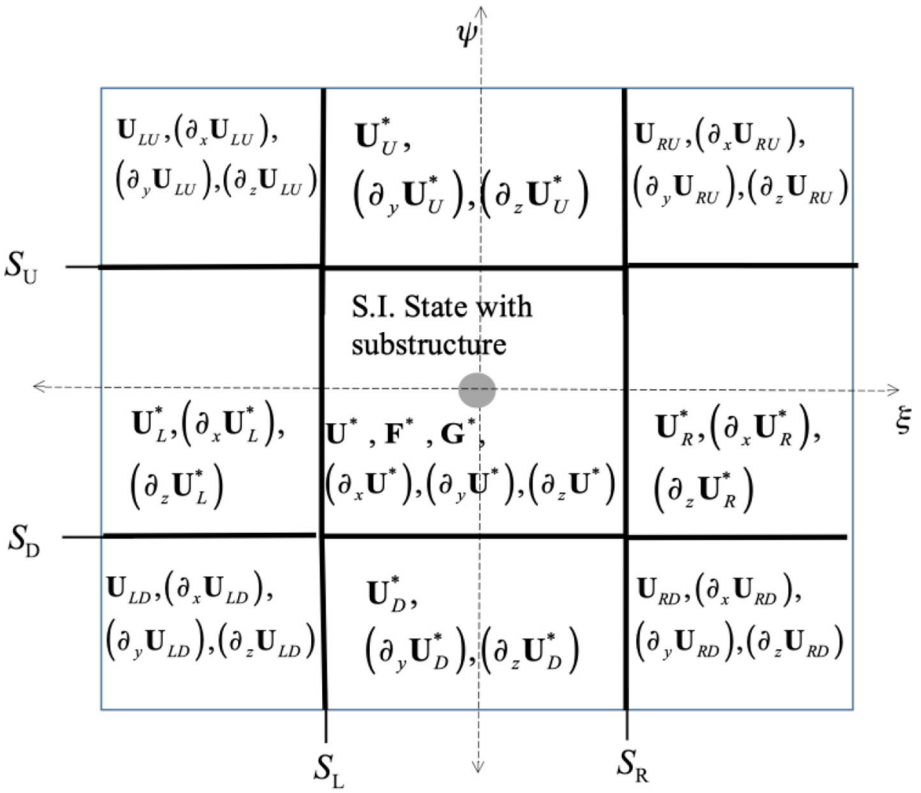

Fig. 4 Input data for the multidimensional GRP—the four input states from Fig. 3a now come in with their gradients in all directions. We also show the resolved states of the one-dimensional Riemann problems and the minimum number of gradients that we should retain in those resolved states. The strongly-interacting state now has all three gradients

We now describe how one transitions from a multidimensional Riemann solver to a multidimensional GRP solver. Figure 4 shows the input data for the multidimensional GRP—the four input states from Fig. 3a now come in with their gradients in all directions. Therefore, along with the state $\mathbf{U}_{RU}$ we also have its three spatial gradients $\partial_x\mathbf{U}_{RU}$, $\partial_y\mathbf{U}_{RU}$, $\partial_z\mathbf{U}_{RU}$. These gradients can be obtained from any higher order reconstruction in the neighbouring right-up zone.

Figure 4 shows that similar gradients can be obtained from other neighbouring zones. We also show the resolved states associated with the one-dimensional Riemann problems and the minimum number of gradients that we should retain in those resolved states. The strongly-interacting state now has all three gradients. Once the gradients have been obtained in the strongly-interacting state, they can be used to obtain the "in-the-small" time-evolution of the strongly-interacting state. This can be done in the sense of a Lax-Wendroff procedure, resulting in a multidimensional GRP solver that is second order in time.

First, we focus on the resolved states, represented by $\mathbf{U}^*_U$, $\mathbf{U}^*_D$, $\mathbf{U}^*_R$, $\mathbf{U}^*_L$ in, Fig. 4 that emerge when we apply the one-dimensional Riemann solvers taking two input states at a time from four input states. For example, we can obtain the resolved state $\mathbf{U}^*_U$ taking $\mathbf{U}_{RU}$ and $\mathbf{U}_{LU}$ as inputs and using Eq. (3.3) and it is given by:

$$\mathbf{U}_U^* = -\frac{1}{S_R - S_L}\Big[(\tilde{\boldsymbol{A}} - S_R\mathbf{I})\mathbf{U}_{RU} - (\tilde{\boldsymbol{A}} - S_L\mathbf{I})\mathbf{U}_{LU}\Big], \quad \mathbf{I}: \text{Identity Matrix.} \tag{3.6}$$

Now that we have obtained $\mathbf{U}_U^*$, we can also find the associated y-flux in the upper resolved state as $\boldsymbol{G}_U^* = \tilde{\boldsymbol{B}}\mathbf{U}_U^*$.

We can see from Fig. 4, that we already have $\partial_y \mathbf{U}_{RU}$ and $\partial_y \mathbf{U}_{LU}$. Also, as we deal with a linear hyperbolic system with constant extremal speeds S_R and S_L here, we can obtain the following expressions for partial derivative of the resolved state in y direction using Eq. (3.4):

$$\partial_y \mathbf{U}_U^* = -\frac{1}{S_R - S_L}\Big[(\tilde{\boldsymbol{A}} - S_R\mathbf{I})\ \partial_y\mathbf{U}_{RU} - (\tilde{\boldsymbol{A}} - S_L\mathbf{I})\ \partial_y\mathbf{U}_{LU}\Big]. \tag{3.7}$$

Similarly, we can obtain the partial derivative of the resolved state with respect to z using Eq. (3.4) and it is given by

$$\partial_z \mathbf{U}_U^* = -\frac{1}{S_R - S_L}\Big[(\tilde{\boldsymbol{A}} - S_R\mathbf{I})\ \partial_z\mathbf{U}_{RU} - (\tilde{\boldsymbol{A}} - S_L\mathbf{I})\ \partial_z\mathbf{U}_{LU}\Big]. \tag{3.8}$$

We can obtain analogous results for $\mathbf{U}_D^*$ by replacing U with D in the subscript of Eqs. (3.6) to (3.8).

Now let us focus on the states $\mathbf{U}_{RU}$ and $\mathbf{U}_{RD}$ and the associated extremal speeds S_U, S_D in Fig. 4 and we have a y-directional Riemann problem. Using Eq. (3.3), we obtain

$$\mathbf{U}_R^* = -\frac{1}{S_U - S_D}\Big[(\tilde{\boldsymbol{B}} - S_U\mathbf{I})\mathbf{U}_{RU} - (\tilde{\boldsymbol{B}} - S_D\mathbf{I})\mathbf{U}_{RD}\Big]. \tag{3.9}$$

We have obtained $\mathbf{U}_R^*$, we can also find the associated x-flux in the right resolved state as $\boldsymbol{F}_R^* = \tilde{\boldsymbol{A}}\mathbf{U}_R^*$. The expressions (3.3) and (3.4) are used in the next section to develop a complete multidimensional GRP-based solver.

We can see from Fig. 4 that we already have $\partial_y \mathbf{U}_{RU}$ and $\partial_y \mathbf{U}_{RD}$. Therefore, for a linear hyperbolic system and constant speeds S_U and S_D, we can obtain x and z derivative of the resolved state U_R using Eq. (3.4).

$$\partial_x \mathbf{U}_R^* = -\frac{1}{S_U - S_D}\Big[(\tilde{\boldsymbol{B}} - S_U\mathbf{I})\ \partial_x\mathbf{U}_{RU} - (\tilde{\boldsymbol{B}} - S_D\mathbf{I})\ \partial_x\mathbf{U}_{RD}\Big], \tag{3.10}$$

$$\partial_z \mathbf{U}_R^* = -\frac{1}{S_U - S_D}\Big[(\tilde{\boldsymbol{B}} - S_U\mathbf{I})\ \partial_z\mathbf{U}_{RU} - (\tilde{\boldsymbol{B}} - S_D\mathbf{I})\ \partial_z\mathbf{U}_{RD}\Big]. \tag{3.11}$$

We can obtain analogous results for $\mathbf{U}_L^*$ by replacing R with L in the subscript of Eqs. (3.9) to (3.11).

At this point, we have all the necessary expressions to obtain the strongly-interacting state $\mathbf{U}^*$ as depicted in Fig. 4 and it can be obtained using Equation (12) in [27],

$$\begin{aligned}\mathbf{U}^* = -\frac{1}{2}\Bigg(&\frac{1}{S_R - S_L}\Big[(\tilde{\boldsymbol{A}} - S_R\mathbf{I})\mathbf{U}_R^* - (\tilde{\boldsymbol{A}} - S_L\mathbf{I})\mathbf{U}_L^*\Big] \\ &+ \frac{1}{S_U - S_D}\Big[(\tilde{\boldsymbol{B}} - S_U\mathbf{I})\mathbf{U}_U^* - (\tilde{\boldsymbol{B}} - S_D\mathbf{I})\mathbf{U}_D^*\Big]\Bigg).\end{aligned} \tag{3.12}$$

From Eq. (3.12), we can obtain $\boldsymbol{F}^* = \tilde{\boldsymbol{A}}\mathbf{U}^*$ and $\boldsymbol{G}^* = \tilde{\boldsymbol{B}}\mathbf{U}^*$. Also, Eq. (3.12) can be formally differentiated in the z-direction to obtain $\partial_z \mathbf{U}^*$ as follows:

$$\partial_z \mathbf{U}^* = -\frac{1}{2}\Bigg(\frac{1}{S_R - S_L}\Big[(\tilde{\boldsymbol{A}} - S_R\mathbf{I})\partial_z \mathbf{U}_R^* - (\tilde{\boldsymbol{A}} - S_L\mathbf{I})\partial_z \mathbf{U}_L^*\Big] + \frac{1}{S_U - S_D}\Big[(\tilde{\boldsymbol{B}} - S_U\mathbf{I})\partial_z \mathbf{U}_U^* - (\tilde{\boldsymbol{B}} - S_D\mathbf{I})\partial_z \mathbf{U}_D^*\Big]\Bigg). \tag{3.13}$$

For the x- and y-gradients of the strongly-interacting state, a more sophisticated treatment is described in the ensuing paragraphs. For those who seek the x- and y-fluxes associated with the state $\mathbf{U}^*$, please see Equations (13) and (14) of [27].

We now focus on introducing x- and y-gradients in the strongly-interacting state in Fig. 4. Consider a general linear hyperbolic system with variation in the x-direction. It can be formally written as

$$\partial_t \mathbf{U} + \tilde{\boldsymbol{A}}\partial_x \mathbf{U} = 0.$$

If we differentiate that equation with respect to the x-coordinate, it becomes

$$\partial_t(\partial_x \mathbf{U}) + \tilde{\boldsymbol{A}}\partial_x(\partial_x \mathbf{U}) = 0.$$

We see, therefore, that the x-gradient of the solution vector also satisfies a linearized Riemann problem with the same foliation of waves as the original linear hyperbolic system. This insight was first used by Titarev and Toro in [48] to obtain the gradient of the resolved state inside the Riemann fan. It also explains why we will only need $\partial_x \mathbf{U}_R^*$ and $\partial_x \mathbf{U}_L^*$ to obtain $\partial_x \mathbf{U}^*$. Note, however, from an examination of Eq. (3.10) that $\partial_x \mathbf{U}_R^*$ and $\partial_x \mathbf{U}_L^*$ do indeed depend on all the x-gradients from all the input states. Consequently, we obtain $\partial_x \mathbf{U}^*$ via a genuinely multidimensional contribution from all the input states. Similarly, we will only need $\partial_y \mathbf{U}_R^*$ and $\partial_y \mathbf{U}_L^*$ to obtain $\partial_y \mathbf{U}^*$. In the next two paragraphs, we make this process explicit. We will subsequently provide all possible details using CED as an example.

From the discussion in the previous paragraph, we have understood that the longitudinal (i.e. x-directional) gradients of the strongly-interacting state also satisfy the linear system

$$\partial_t(\partial_x \mathbf{U}^*) + \tilde{\boldsymbol{A}}\partial_x(\partial_x \mathbf{U}^*) = 0, \tag{3.14}$$

with the initial conditions:

$$\partial_x \mathbf{U}^*|_{t=0} = \partial_x \mathbf{U}_L^* \quad \text{if } x < 0$$
$$\partial_x \mathbf{U}^*|_{t=0} = \partial_x \mathbf{U}_R^* \quad \text{if } x > 0.$$

We now use the Titarev-Toro-style linearization. Because the characteristic matrix is constant, the solution of the linear system is easily found. Within the context of the linearization in Eq. (3.14), we obtain the solution

$$\partial_x \mathbf{U}^* = \begin{cases} \partial_x \mathbf{U}_L^* & \text{when } S_L \geq 0 \\ \frac{1}{2}\Big[\partial_x \mathbf{U}_L^* + \partial_x \mathbf{U}_R^*\Big] + \frac{1}{2}\sum_{m=1}^{m_x} \alpha_x^m r_x^m - \frac{1}{2}\sum_{m=m_x+1}^{M} \alpha_x^m r_x^m & \text{when } S_L < 0 < S_R \\ \partial_x \mathbf{U}_R^* & \text{when } S_R \leq 0 \end{cases}$$
$$\text{with } \alpha_x^m \equiv l_x^m \cdot \big[\partial_x \mathbf{U}_R^* - \partial_x \mathbf{U}_L^*\big]. \tag{3.15}$$

In the above equation, the eigenvalues $\lambda_x^m,\ m = 1, 2, 3, \ldots M$ of the left eigenvectors $l_x^m,\ m = 1, 2, 3, \ldots M$ and the right eigenvectors $r_x^m,\ m = 1, 2, 3, \ldots M$ are obtained from the characteristic matrix $\tilde{\boldsymbol{A}}$. In Eq. (3.15) m_x is defined to be the unique wave for which we have $\lambda_x^{m_x} < 0 < \lambda_x^{m_x+1}$. This completes our description of $(\partial_x \mathbf{U}^*)$. [We also point out that the omission of a factor of half in front of the eigenvectors in Equation (2.19) of [62] is indeed an error, and this paper fixes the deficiency in the form of an erratum to that prior paper.]

Analogous to the discussion in the previous paragraph, the *longitudinal (i.e. y-directional) gradients of the strongly-interacting state* also satisfy the linear system

$$\partial_t(\partial_y \mathbf{U}^*) + \tilde{\boldsymbol{B}}\partial_y(\partial_y \mathbf{U}^*) = 0, \tag{3.16}$$

with the initial conditions:

$$\begin{aligned} \partial_y \mathbf{U}^*|_{t=0} &= \partial_y \mathbf{U}_D^* \quad \text{if } y < 0 \\ \partial_y \mathbf{U}^*|_{t=0} &= \partial_y \mathbf{U}_U^* \quad \text{if } y > 0. \end{aligned}$$

As before, we use the Titarev-Toro-style linearization. Because the characteristic matrix is constant, the solution of the linear system is easily found. Within the context of the linearization in Eq. (3.16), we obtain the solution

$$\partial_y \mathbf{U}^* = \begin{cases} \partial_y \mathbf{U}_D^* & \text{when } S_D \geq 0 \\ \frac{1}{2}\left[\partial_y \mathbf{U}_D^* + \partial_y \mathbf{U}_U^*\right] + \frac{1}{2}\sum_{m=1}^{m_y} \alpha_y^m r_y^m - \frac{1}{2}\sum_{m=m_y+1}^{M} \alpha_y^m r_y^m & \text{when } S_D < 0 < S_U \\ \partial_y \mathbf{U}_U^* & \text{when } S_U \leq 0 \end{cases}$$

$$\text{with } \alpha_y^m \equiv l_y^m \cdot \left[\partial_y \mathbf{U}_U^* - \partial_y \mathbf{U}_D^*\right]. \tag{3.17}$$

In the above equation, the eigenvalues $\lambda_y^m,\ m = 1, 2, 3, \ldots M$ the left eigenvectors $l_y^m,\ m = 1, 2, 3, \ldots M$ and the right eigenvectors $r_y^m,\ m = 1, 2, 3, \ldots M$ are obtained from the characteristic matrix $\tilde{\boldsymbol{B}}$. In Eq. (3.17) m_y is defined to be the unique wave for which we have $\lambda_y^{m_y} < 0 < \lambda_y^{m_y+1}$. This completes our description of $(\partial_y \mathbf{U}^*)$.

For CED, the eigenvalues and orthonormal eigenvectors have been documented in [15]. Two of the waves in this system become non-evolutionary because they correspond to the constraints. The case where the permittivity and permeability are diagonal is very important. In that case, we give explicit expressions for $(\partial_x \mathbf{U}^*)$ and $(\partial_y \mathbf{U}^*)$. For $(\partial_x \mathbf{U}^*)$, we have

$$\partial_x \mathbf{U}^* = \frac{1}{2}\left(\partial_x \mathbf{U}_L^* + \partial_x \mathbf{U}_R^*\right) + \frac{1}{2}\begin{bmatrix} 0 \\ -\sqrt{\frac{\tilde{\mu}_{zz}}{\tilde{\varepsilon}_{yy}}}\left((\partial_x \mathbf{U}_R^*)_6 - (\partial_x \mathbf{U}_L^*)_6\right) \\ \sqrt{\frac{\tilde{\mu}_{yy}}{\tilde{\varepsilon}_{zz}}}\left((\partial_x \mathbf{U}_R^*)_5 - (\partial_x \mathbf{U}_L^*)_5\right) \\ 0 \\ \sqrt{\frac{\tilde{\varepsilon}_{zz}}{\tilde{\mu}_{yy}}}\left((\partial_x \mathbf{U}_R^*)_3 - (\partial_x \mathbf{U}_L^*)_3\right) \\ -\sqrt{\frac{\tilde{\varepsilon}_{yy}}{\tilde{\mu}_{zz}}}\left((\partial_x \mathbf{U}_R^*)_2 - (\partial_x \mathbf{U}_L^*)_2\right) \end{bmatrix}. \tag{3.18}$$

In the above equation, $(\partial_x \mathbf{U}^*_{(\cdot)})_i$ denotes the i-the component of the corresponding vector.

$$\partial_y \mathbf{U}^* = \frac{1}{2}\Big(\partial_y \mathbf{U}^*_D + \partial_y \mathbf{U}^*_U\Big) + \frac{1}{2}\begin{bmatrix} \sqrt{\frac{\tilde{\mu}_{zz}}{\tilde{\varepsilon}_{xx}}}\Big((\partial_y \mathbf{U}^*_U)_6 - (\partial_y \mathbf{U}^*_D)_6\Big) \\ 0 \\ -\sqrt{\frac{\tilde{\mu}_{xx}}{\tilde{\varepsilon}_{zz}}}\Big((\partial_y \mathbf{U}^*_U)_4 - (\partial_y \mathbf{U}^*_D)_4\Big) \\ -\sqrt{\frac{\tilde{\varepsilon}_{zz}}{\tilde{\mu}_{xx}}}\Big((\partial_y \mathbf{U}^*_U)_3 - (\partial_y \mathbf{U}^*_D)_3\Big) \\ 0 \\ \sqrt{\frac{\tilde{\varepsilon}_{xx}}{\tilde{\mu}_{zz}}}\Big((\partial_x \mathbf{U}^*_U)_1 - (\partial_x \mathbf{U}^*_D)_1\Big) \end{bmatrix}. \tag{3.19}$$

The above two equations show us how easy it is to obtain the gradients in the strongly-interacting state.

3.3 A GRP solver Without any Source Term

In its most rudimentary form, a multidimensional GRP solver is used as follows. We hand in the four states and their gradients as inputs to the multidimensional GRP at time t^n. The GRP in turn produces the strongly-interacting state $\mathbf{U}^*$ and its gradients $\partial_x \mathbf{U}^*_U$, $\partial_y \mathbf{U}^*_U$ and $\partial_z \mathbf{U}^*_U$ at each t^n. However, a GRP solver should enable us to take a temporally second order accurate time update to a time $t^{n+1} = t^n + \Delta t$ in one call to the GRP solver. As a result, we want the time-centered solution at a time of $t^n + \Delta t/2$. This is obtained by a Lax-Wendroff-like procedure as follows:

$$\mathbf{U}^{*,1/2} = \mathbf{U}^* - \frac{\Delta t}{2}\Big[\tilde{\boldsymbol{A}}(\partial_x \mathbf{U}^*) + \tilde{\boldsymbol{B}}(\partial_y \mathbf{U}^*) + \tilde{\boldsymbol{C}}(\partial_z \mathbf{U}^*)\Big]. \tag{3.20}$$

With $\mathbf{U}^{*,1/2}$ in hand, we can easily obtain time-centered electric and magnetic fields at the edges of the mesh. This enables us to find the electric field and magnetic field components at the edges of the mesh with the result that Eq. (2.11) then be used to make a single-step, second order in time update.

3.4 A GRP Solver for Linear Systems with Stiff Linear Source

The output from the GRP solver will be a state $\mathbf{U}^{*,1/2}$ updated to a time $t^{n+1/2}$ at the edges of the mesh, as discussed in the previous sub-section. This state has to be at least first order accurate in time for the overall time update in Eq. (2.11) to be second order accurate in time. Now let us consider the inclusion of the source term in Eq. (3.2). We can write the update that is analogous to Eq. (3.20), but this time we write it formally so that the effect of the source term is included at least up to first order of accuracy. We therefore write

$$\mathbf{U}^{*,1/2} = \mathbf{g}(\Delta t\ \tilde{\boldsymbol{\Sigma}})\Big[\mathbf{U}^* - \frac{\Delta t}{2}\Big[\tilde{\boldsymbol{A}}(\partial_x \mathbf{U}^*) + \tilde{\boldsymbol{B}}(\partial_y \mathbf{U}^*) + \tilde{\boldsymbol{C}}(\partial_z \mathbf{U}^*)\Big]\Big]. \tag{3.21}$$

Here $\mathbf{g}(\Delta t\ \tilde{\boldsymbol{\Sigma}})$ is a matrix function that depends only on the matrix $\Delta t\ \tilde{\boldsymbol{\Sigma}}$ because the source terms are linear. The matrix function can consist of any reasonable approximation

of $e^{-(\frac{\Delta t}{2}\ \tilde{\mathbf{\Sigma}})}$. In the next paragraph, we will examine the concept of L-stability in CED. We will then specialize $\mathbf{g}(\Delta t\ \tilde{\mathbf{\Sigma}})$ to ensure L-stability so that the overall timestep has this very beneficial stability property.

The update in Eq. (2.11) can be formally written as

$$\mathbf{U}^{n+1} = \mathbf{U}^n - \Delta t\ \tilde{\mathbf{\Sigma}}\ \mathbf{U}^{*,1/2} - \Delta t \mathbf{R}(\mathbf{U}^{*,1/2}), \tag{3.22}$$

where $\mathbf{U}^{*,1/2}$, $\Delta t\ \tilde{\mathbf{\Sigma}}\ \mathbf{U}^{*,1/2}$ and $\mathbf{R}(\mathbf{U}^{*,1/2})$ represent the output state from the multidimensional GRP updated to a time $t^n + \Delta t/2$ at the edges of the mesh, the source terms and a discrete representation of the curl type operator in Eq. (2.11) respectively. In fairness, the facial currents in Eq. (2.11) are obtained by averaging the currents provided at the edges of the mesh by the multidimensional GRP. However, that point of detail does not affect the following analysis. The demonstration of L-stability does not rely on the form of the curl-type terms, and so we will ignore the presence of the curl-type terms for the rest of this formal demonstration of L-stability. In other words, to demonstrate L-stability, we will ignore terms with any spatial gradients and focus only on the source terms. When all spatial gradients are set to zero, we have $\mathbf{U}^* = \mathbf{U}^n$. Ignoring all spatial gradients, Eqs. (3.21) and (3.22) give us

$$\mathbf{U}^{n+1} = \Big[\mathbf{I} - \Delta t\ \tilde{\mathbf{\Sigma}}\ \mathbf{g}(\Delta t\ \tilde{\mathbf{\Sigma}})\Big]\mathbf{U}^n = \mathbf{G}(\tilde{\Sigma}\Delta t)\mathbf{U}^n, \tag{3.23}$$

where $\mathbf{G}(\cdot)$ is the overall amplification factor of the scheme.

The effect of finite conductivity in Maxwell's equations is such that, if the spatial gradients do not act, and if the entire system is governed by non-zero conductivity, then the end result after a significantly long time interval should be a zero electric displacement and a zero magnetic induction. In other words, as $\Delta t\ \tilde{\mathbf{\Sigma}} \to \infty$, we want $\Big[\mathbf{I} - \Delta t\ \tilde{\mathbf{\Sigma}}\ \mathbf{g}(\Delta t\ \tilde{\mathbf{\Sigma}})\Big] \to 0$. This is a physics-based interpretation of L-stability. The matrix function $\mathbf{g}(\Delta t\ \tilde{\mathbf{\Sigma}})$ that we choose should reflect that fact. Notice that $\tilde{\mathbf{\Sigma}}$ is either a non-negative diagonal matrix, or it can be diagonalized into such a form via a similarity transformation. As a result, we can define $\chi \equiv \Delta t\ \tilde{\mathbf{\Sigma}}$ and simplify our analysis by treating $\tilde{\mathbf{\Sigma}}$ as a scalar. L-stability is therefore equivalent to demanding that

$$\lim_{\chi \to \infty} \chi \mathbf{g}(\chi) = 1. \tag{3.24}$$

In the next three paragraphs we explore different reasonable forms for $\mathbf{g}(\chi)$ so as to finally obtain an L-stable formulation. Figure 5 shows the overall amplification factor $\mathbf{G}(\chi) = 1 - \chi\mathbf{g}(\chi)$ for different choices.

Let us first examine the exact solution operator of the stiff source term. In that case, and with all gradients set to zero, for Eq. (3.21) we obtain the following:

$$\mathbf{U}^{*,1/2} = e^{-(\Delta t/2\ \tilde{\mathbf{\Sigma}})}\mathbf{U}^n \qquad \text{with } \mathbf{g}(\chi) \equiv e^{-\chi/2}. \tag{3.25}$$

For this choice, we have

$$\lim_{\chi \to \infty} \chi \mathbf{g}(\chi) = \lim_{\chi \to \infty} \chi e^{-\chi/2} = 0. \tag{3.26}$$

So we see that the exact solution operator of the stiff source term does not satisfy the L-stability criteria (3.24) and as a result the overall scheme is not L-stable. We might think that the exact evolution operator for the source term should be an ideal choice, but this is not the case when we consider the overall scheme.

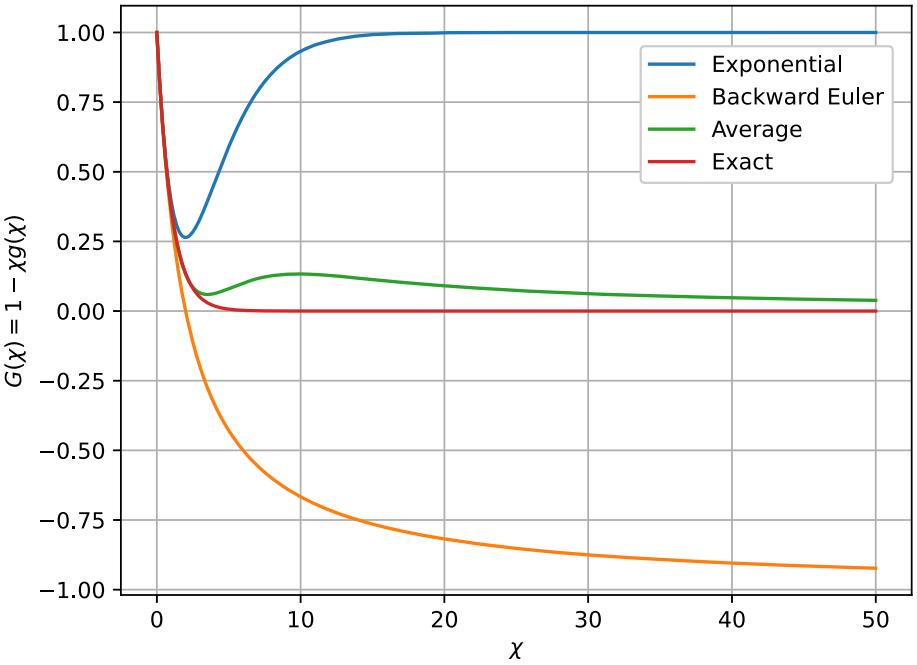

Fig. 5 Amplification factor as a function of $\chi = \tilde{\boldsymbol{\Sigma}}\Delta t$. We show that an exact solution as well as the backward Euler solution do not result in an overall time update strategy that has the L-stability property. However, the arithmetic average of the two solutions leads to an overall update strategy that is indeed L-stable. The exact solution is also shown

Let us next examine the backward Euler solution. In that case, and with all gradients set to zero, we have the following form for Eq. (3.21)

$$\mathbf{U}^{*,1/2} = \left[\mathbf{I} + \frac{\Delta t}{2}\tilde{\boldsymbol{\Sigma}}\right]^{-1}\mathbf{U}^{n} \qquad \text{with } \mathbf{g}(\chi) \equiv \frac{1}{1+\chi/2}. \tag{3.27}$$

For this choice, we have

$$\lim_{\chi\to\infty} \chi\mathbf{g}(\chi) = \lim_{\chi\to\infty} \frac{\chi}{1+\chi/2} = 2. \tag{3.28}$$

Therefore, we see that the overall amplification factor of the scheme with backward Euler time-stepping $\lim_{\chi\to\infty} \mathbf{G}(\chi) = \lim_{\chi\to\infty}(1-\chi\mathbf{g}(\chi)) = -1$.

While the exact and backward Euler solution are not L-stable, the two options begin to hint towards an optimal choice. Since both the exact and the backward Euler solution would give us an overall scheme that is second order accurate in time, an arithmetic average of the two would also give us a second order accuracy in time. If we take the average of these two options, we obtain the following form for Eq. (3.21)

$$\mathbf{U}^{*,1/2} = \frac{1}{2}\left[\mathrm{e}^{-(\frac{\Delta t}{2}\tilde{\boldsymbol{\Sigma}})} + \left(\mathbf{I} + \frac{\Delta t}{2}\tilde{\boldsymbol{\Sigma}}\right)^{-1}\right]\left[\mathbf{U}^{*} - \frac{\Delta t}{2}\left(\tilde{\boldsymbol{A}}(\partial_x\mathbf{U}^{*}) + \tilde{\boldsymbol{B}}(\partial_y\mathbf{U}^{*}) + \tilde{\boldsymbol{C}}(\partial_z\mathbf{U}^{*})\right)\right]. \tag{3.29}$$

Now if we set all the gradients to zero, we obtain

$$\mathbf{U}^{*,1/2} = \frac{1}{2}\Big[\mathrm{e}^{-(\Delta t/2\ \tilde{\mathbf{\Sigma}})} + \Big(\mathbf{I} + \frac{\Delta t}{2}\tilde{\mathbf{\Sigma}}\Big)^{-1}\Big]\mathbf{U}^{n}, \tag{3.30}$$

and thus

$$\mathbf{g}(\chi) = \frac{1}{2}\Big(\mathrm{e}^{-(\frac{\chi}{2})} + \frac{1}{1+\chi/2}\Big). \tag{3.31}$$

For this choice we have

$$\lim_{\chi\to\infty} \chi\mathbf{g}(\chi) = \lim_{\chi\to\infty} \frac{\chi}{2}\Big(\mathrm{e}^{-(\frac{\chi}{2})} + \frac{1}{1+\chi/2}\Big) = 1. \tag{3.32}$$

Therefore, we see that we have found an L-stable scheme and Eq. (3.29) gives us an expression of the final, successful choice of an overall scheme.

4 Pointwise Strategy for Implementation

The following steps will result in a one-step, GRP-based, second order accurate in space and time FVTD scheme for CED which preserves the global constraints and is L-stable in the presence of stiff linear source terms.

1. The primal variables of the scheme are facially-averaged normal components of the electric displacement vector field and the magnetic induction vector field, as shown in Fig. 1. These components give us a second order accurate reconstruction of electric displacement vector field and the magnetic induction vector fields following Section III of [15].
2. Focus on each edge center of a Cartesian mesh. Consider the four zones that abut this edge. Use the reconstructed fields to obtain the four input states to the multidimensional GRP. Because the reconstruction from the previous step also enables us to obtain the gradients in all directions from those four states, we also provide these gradients as inputs to the GRP.
3. Use Eq. (3.5) to obtain $S_R,\ S_L,\ S_U,\ S_D$. This enables us to identify the multidimensional wave model, shown in the left panel of Fig. 3.
4. Use Eqs. (3.6),(3.8) and (3.7) to obtain $\mathbf{U}^*_U$ and its gradients in the y- and z-directions. Do analogously for $\mathbf{U}^*_D$.
5. Use Eqs. (3.9),(3.10) and (3.11) to obtain $\mathbf{U}^*_R$ and its gradients in the x- and z-directions. Do analogously for $\mathbf{U}^*_L$.
6. Use Eqs. (3.12) and (3.13) to obtain the strongly-interacting state U^* and its gradient in the z-direction.
7. Use Eqs. (3.18) and (3.19) to obtain the gradients of the strongly-interacting state in the x and y-directions. Please note that Eqs. (3.18) and (3.19) are just specialized forms of Eqs. (3.15) and (3.17) respectively.
8. If there are no source terms, use Equation (3.20). If source terms are present, use Equation (3.29). This gives us the time-centered states at the edges of the mesh that can be used to construct the curl-type operators in Eq. (2.11).
9. If sources are present, obtain the facial current densities by averaging the edge-centered values of the same. This gives us an L-stable treatment of the stiff source terms.
10. Make the update in Eq. (2.11). This completes our description of a spatially and temporally second order accurate, globally constraint-preserving, FVTD time update.

5 Accuracy Analysis

5.1 Propagation of a Plane Electromagnetic Wave in Two Dimensions

In this test problem, we study the propagation of a plane electromagnetic wave through vacuum along the north-east diagonal direction of a two dimensional Cartesian domain spanning $[-0.5, 0.5] \times [-0.5, 0.5]$ m^2. For a detailed description of the problem set up and the electromagnetic field initialization, the readers are referred to [14] for three dimensional version of this test problem and [15] for the two dimensional version of this test problem. Since the analytical solution is known at any space and time, this test problem is very suitable for accuracy analysis. We use a CFL of 0.45 and enforce a periodic boundary condition for this problem. The simulation has been run till a time of 3.5×10^{-9} s second and a uniform mesh has been used in all the runs presented here. Table 1 shows the accuracy analysis for this test problem. We can see the algorithm meets it designed accuracy for this problem.

5.2 Compact Gaussian Electromagnetic Pulse Incident on a Refractive Disk

In this two dimensional test problem, we study the propagation of a compact Gaussian electromagnetic pulse that is incident on a refractive disk of refractive index 3.0. The simulation has been performed on a computational domain spanning $[-7.0, 7.0] \times [-7.0, 7.0]$ m^2. The refractive disk of radius 0.75m is placed at the center of the computational domain. More details about this problem set up and initialization of the compact Gaussian pulse can be found in [15].

This simulation has been run with a CFL of 0.45 and continuative boundary condition is enforced for this problem. We stop this simulation at a final time of 2.33×10^{-8} s. For the simulations presented here, we use a uniform mesh with zones ranging from 120×120 to 960×960. Since the problem has no analytic solution, we use a 1920×1920 mesh solution as the reference solution for computing the L^1 and L^∞ errors. Table 2 shows the result of the accuracy analysis for this problem. The results show that, even for this problem, our algorithm meets its design accuracy.

Table 1 Accuracy analysis for multidimensional GRP scheme for the propagation of an electromagnetic wave in vacuum. A CFL of 0.45 was used. The errors and accuracy in the y-component of the electric displacement vector and z-component of the magnetic induction are shown

$N_x \times N_y$	$\|D_y^h - D_y\|_{L^1}$	Ord	$\|D_y^h - D_y\|_{L^\infty}$	Ord
16×16	9.8208e−05	–	1.5146e−04	–
32×32	2.2130e−05	2.15	3.4776e−05	2.12
64×64	5.5153e−06	2.00	8.6592e−06	2.01
128×128	1.3850e−06	1.99	2.1753e−06	1.99
	$\|B_z^h - B_z\|_{L^1}$	Ord	$\|B_z^h - B_z\|_{L^\infty}$	Ord
16×16	4.9235e−02	–	7.8128e−02	–
32×32	1.1492e−02	2.10	1.8000e−02	2.12
64×64	2.8693e−03	2.00	4.5064e−03	2.00
128×128	7.2069e−04	1.99	1.1320e−03	1.99

Table 2 Convergence of error for multidimensional GRP scheme for the propagation of a compact Gaussian electromagnetic pulse that is incident on a refractive disk. A CFL of 0.45 was used. The errors and accuracy in the y-component of the electric displacement vector and z-component of the magnetic induction are shown

$N_x \times N_y$	$\|D_y^h - D_y\|_{L^1}$	Ord	$\|D_y^h - D_y\|_{L^\infty}$	Ord
120 × 120	4.5549e−05	–	1.7269e−02	–
240 × 240	2.8758e−05	0.66	1.7414e−02	−0.01
480 × 480	1.1046e−05	1.38	6.3582e−03	1.45
960 × 960	2.3549e−06	2.23	1.2758e−03	2.32
	$\|B_z^h - B_z\|_{L^1}$	Ord	$\|B_z^h - B_z\|_{L^\infty}$	Ord
120 × 120	1.8746e−02	–	2.7283e+00	–
240 × 240	1.0416e−02	0.85	2.9031e+00	−0.09
480 × 480	4.1051e−03	1.34	9.6348e−01	1.59
960 × 960	9.4015e−04	2.13	1.8530e−01	2.38

6 Test Problems

6.1 Refraction of a Compact Electromagnetic Beam by a Dielectric Slab

In this test problem, we study the refraction of a compact electromagnetic beam impinging on a dielectric slab with a permittivity $2.25\epsilon_0$ where ϵ_0 is the permittivity of vacuum. Detailed description about this problem set up and the initialization of the electromagnetic beam can be found in [15].

We perform this simulation on a two dimensional Cartesian domain spanning $[-5.0, 8.0] \times [-2.5, 7.0]\ \mu\text{m}^2$ using a uniform mesh with 1300×950 zones. We use a CFL of 0.45 and stop this simulation at a time of 4.0×10^{-14} s. The result of the simulation is shown in Fig. 6. The top and bottom rows of Fig. 6 shows $B_z,\ D_x,\ D_y$ (from left to right) at the initial and final time respectively. The solid vertical black line indicates the interface of the vacuum and the dielectric slab. We have also plotted inclined solid black line to show the angles of incidence, refraction and reflection. These lines are over-plotted with the field components to guide our eye. Since the angle of incidence is 45° for this case, according to Snell's law, the angle of refraction is 28.12°. We clearly see that our simulation has reproduced the correct value of angle of refraction.

6.2 Total Internal Reflection of a Compact Electromagnetic Beam by a Dielectric Slab

In this test problem, we study the total internal reflection of a compact electromagnetic beam when it is incident on the interface separating a dielectric disk of permittivity $4\epsilon_0$ and vacuum at an angle of 45° which is more than the critical angle 30° for such system. For a detailed description of the problem set up, readers are referred to [15]. We perform this simulation on a rectangular xy-domain using a uniform mesh with 700×850 zones. We use a CFL of 0.45 for this simulation run and stop the simulation at a final time of 5.0×10^{-14} s. The top and bottom rows of Fig. 7 show the initial and final configuration of $B_z,\ D_x,\ D_y$ (from left to right) respectively. The solid vertical black line identifies the interface of the dielectric slab and vacuum. The inclined solid black lines are over-plotted on the field components to guide our eye. The result clearly shows that the incident beam has suffered total internal reflection.

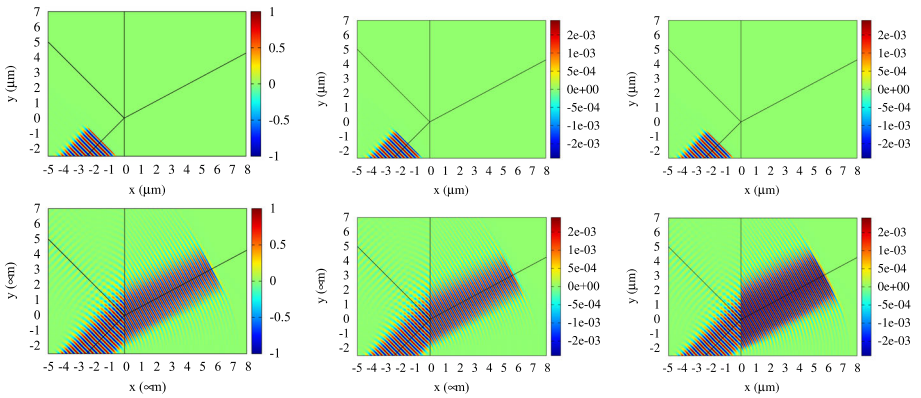

Fig. 6 Refraction of a compact electromagnetic beam by a dielectric slab on a mesh of 1300 × 950 cells. The vertical black line indicates the surface of the dielectric slab. The inclined solid black lines demarcate the angle of incidence, the angle of refraction and the angle of reflection. Top row and bottom row shows B_z, D_x, and D_y at the initial time and at final time 4.0×10^{-14} s respectively

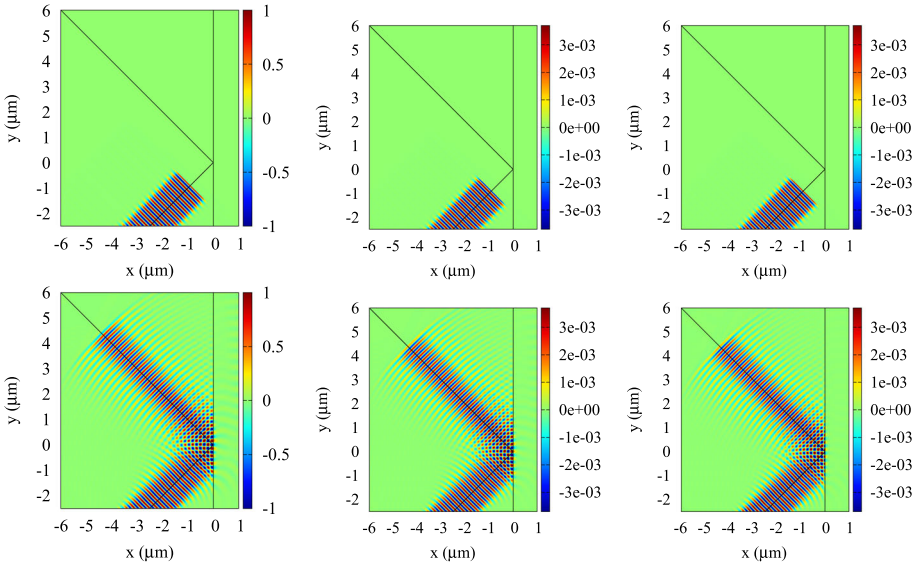

Fig. 7 Total internal reflection of a compact electromagnetic beam by a dielectric slab on a mesh of 700 × 850 cells: The vertical black line indicates the surface of the dielectric slab. The inclined solid black lines demarcate the angle of incidence and the angle of reflection. Top row and bottom row shows B_z, D_x, and D_y at the initial time and at final time 5.0×10^{-14} s respectively

6.3 Compact Electromagnetic Beam Impinging on a Conducting Slab

This test problem is designed to demonstrate the capability of the present algorithm to handle stiff source term. In this test problem, we study the reflection of a compact electromagnetic beam impinging on a slab made up of copper having a conductivity of 5.9×10^7 S m^{-1}. The problem set up is described in detail in [15].

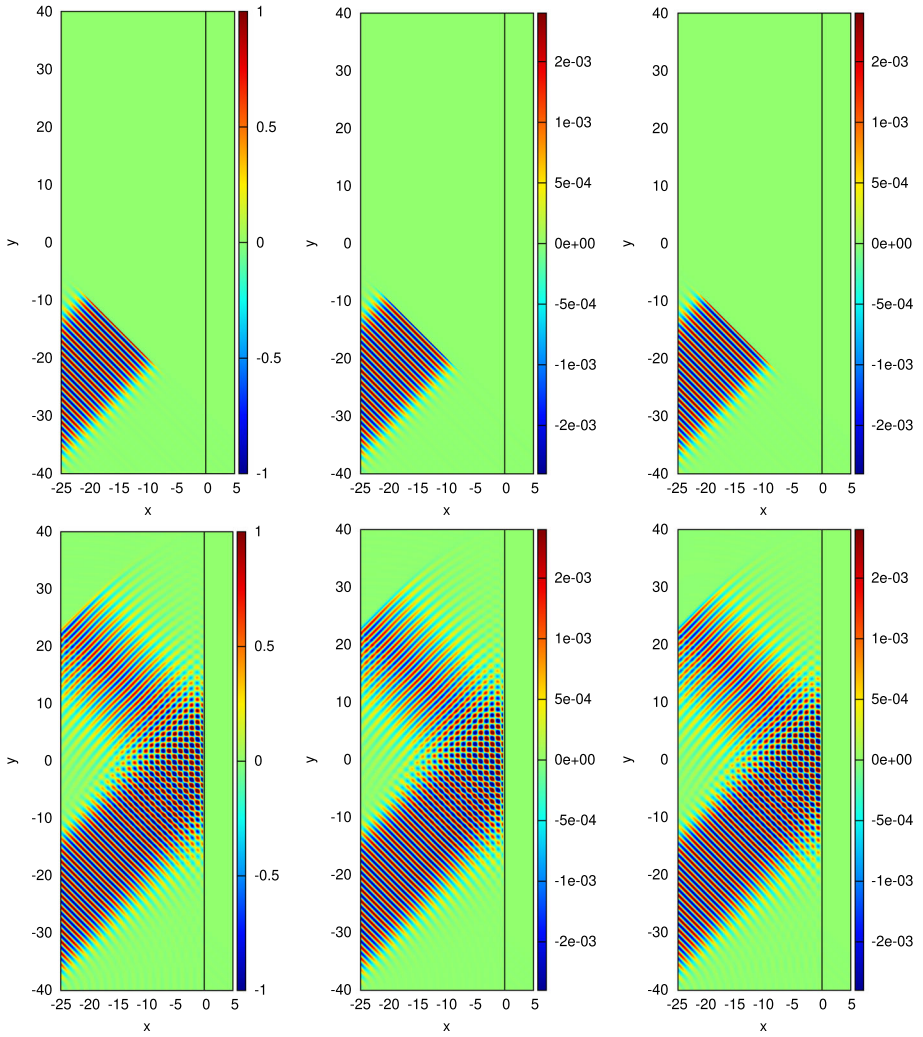

Fig. 8 Compact electromagnetic beam impinging on a conducting slab. Simulation were performed on 1500 $\times$ 4000 cells. The conductor is located at $x = 0$ in the figure and is shown by the vertical black line. Top row: B_z, D_x, and D_y at the initial time. Bottom row: B_z, D_x, and D_y at the final time 1.83×10^{-7} s when the beam has reflected off the surface of the conductor

We perform this simulation on a rectangular xy-domain using a uniform mesh with 1500 $\times$ 4000 zones. For this simulation, we use a CFL of 0.40 and stop the simulation at a time of 1.83×10^{-7} s. The top and bottom rows of Fig. 8 show the initial and final configuration of B_z, D_x, D_y respectively. The solid vertical black line represents the surface of the conducting slab. We can notice the development of interference pattern between the incident wave and the reflected wave close to the surface of the conducting slab.

6.4 Decay of a Sinusoidal Wave Inside a Conductor

Due to the finite skin depth of a conductor, a fraction of the incident wave penetrates it and decays inside it. However, for the meshes used in the previous test problem, we are unable to resolve the skin depth of the copper. Therefore, in this test problem, the simulation set up is designed in a way so that we can resolve the skin depth and study the decay of a sinusoidal wave. The details of the set up and the initialization of the electromagnetic field can be found in [15].

Here, we show results of two one dimensional simulations. In one simulation, we study the decay of the sinusoidal wave inside amorphous carbon having a conductivity of $\sigma = 2.0 \times 10^3\ \mathrm{Sm}^{-1}$ and in the other, we study the same inside copper. For both the simulations, we use a one dimensional domain spanning $[0, 10\delta]$ where δ represents the skin depth of the conductor and a uniform mesh with 100 zones. For carbon, we initialize a sinusoidal wave with frequency $\nu = 1.679 \times 10^{13}$ Hz, which gives $\delta = 3.44 \times 10^{-6}$ m. We use a CFL of 0.90 for this run and stop this simulation at a time of 4.76×10^{-13} s. For copper, we initialize a sinusoidal wave with frequency $\nu = 1.0 \times 10^{13}$ Hz, which gives $\delta = 2.06 \times 10^{-8}$ m. We use a CFL of 0.75 for this run and stop this simulation at a time of4.0×10^{-13} s. Solid black lines in top left and top right panels of Fig. 9 show the variation of B_z with radial distance inside the carbon and copper, respectively. The solid red lines represent the numerically evaluated decaying envelopes. In bottom left and bottom right panels of Fig. 9, we compare the numerically evaluated decaying envelopes (red crosses) with analytically obtained envelopes (blue solid

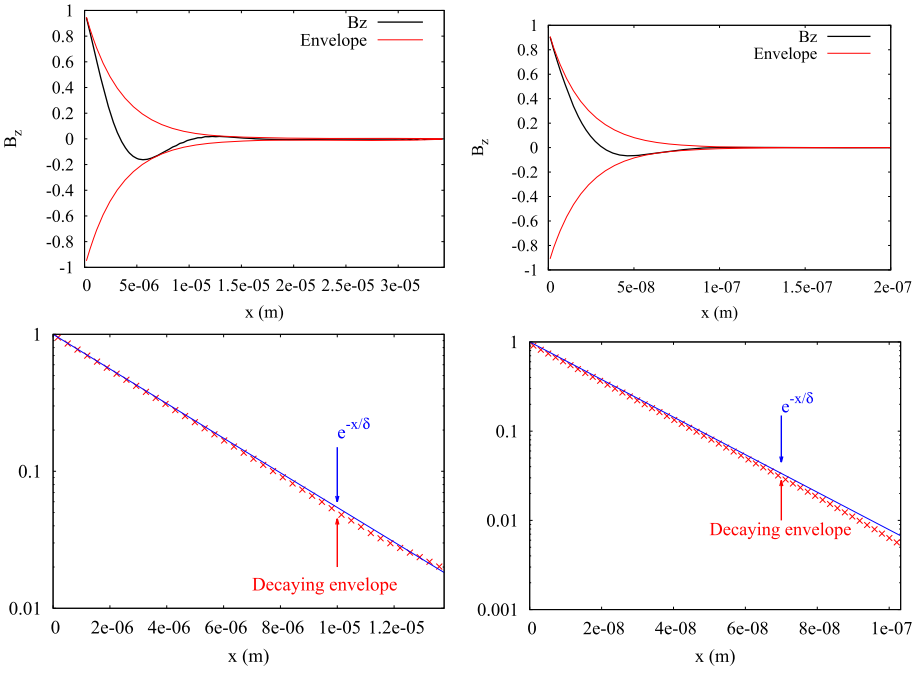

Fig. 9 The top left panel and right panel show the radial variations of B_z (black lines) and the decaying envelopes (red lines) inside carbon and copper, respectively. The bottom left, and the bottom right panel present the structure of the envelopes (red lines) and the theoretical plots on a semi-log scale for carbon and copper, respectively (Color figure online)

line) on a semi-log scale for carbon and copper, respectively. We can see that our numerical results match very well with the analytical results.

6.5 Long-Distance or Long-Time Propagation of Electromagnetic Radiation

Long-time or long-distance wave propagation is crucial for many problems in electrodynamics. Therefore, it is highly desirable to devise CED schemes with minimal dispersive errors. This test problem is designed to demonstrate the numerical dispersion behavior of our numerical scheme. It is also compared with FDTD to prove its superior numerical dispersion behavior over the FDTD scheme. The setup of the problem is analogous to the similar test problem in Section 5.8 of [16].

To replicate the long-time and long-distance propagation of electromagnetic plane waves, we make electromagnetic plane waves propagate in a small computational domain with periodic boundary conditions in multiple cycles. We choose a computational domain that spans $[-\frac{r}{2}, \frac{r}{2}] \times [-\frac{r}{2}, \frac{r}{2}]$ in the xy-plane with $r = 6$ divided into a 180×180 meshes with uniform mesh size and periodic boundary conditions. The exact expression for the electric flux density and the magnetic flux intensity vector fields are given as follows:

$$\boldsymbol{D} = c\,\epsilon_0\big(-n_y \cos(\phi)\hat{e}_x + n_x \cos(\phi)\hat{e}_y\big), \quad \boldsymbol{B} = \cos(\phi)\hat{e}_z$$

where $\phi = \frac{2\pi}{n_y}(n_x x + n_y y - ct)$ and $\hat{\boldsymbol{n}} = n_x\hat{e}_x + n_y\hat{e}_y$ is the direction of propagation of the plane wave.

As it is well known that wave propagation along the mesh lines or 45° is simpler to replicate, we test the dispersion behaviour of our scheme by choosing the direction of wave propagation along $\hat{\boldsymbol{n}} = (\frac{1}{\sqrt{r^2+1}}, \frac{r}{\sqrt{r^2+1}})$ which implies that the plane wave are made to propagate at angle $\tan^{-1}(\frac{1}{r}) = \tan^{-1}(\frac{1}{6}) = 9.462°$ with respect to the y-axis.

Simulation was performed until 4.05×10^{-7} s with a CFL number of 0.45. The final time corresponds to 20 cycles on the periodic mesh, equivalent to propagating the electromagnetic wave over 3600 zones of a uniform mesh.

The left panel of Fig. 10 shows the variation of B_z normalized by the corresponding amplitude of the sinusoid as a function of x along $y = 0$ at the final time. The right panel of Fig. 10 depicts the same, however, as a function of y along $x = 0$. In Fig. 10, results obtained using multidimensional GRP, FDTD are compared with analytical solutions, and

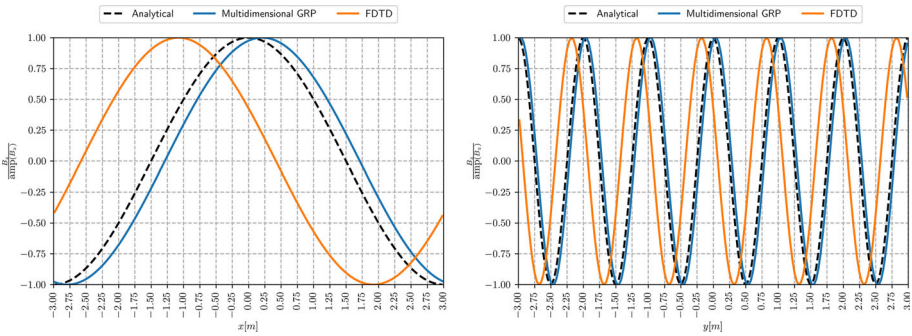

Fig. 10 Long-time propagation of electromagnetic radiation. B_z normalized by the amplitude for multidimensional GRP, FDTD schemes and analytical solution at the final time. Left panel shows the variation along the x-axis at $y = 0$, while the right panel shows the variation along the y-axis at $x = 0$

we can observe that analytical results and multidimensional GRP-computed results are close to each other whereas FDTD-computed results lagged in the left relative to them by 1 m distance. Similar result has also been reported in [16].

7 Conclusions

In this paper, we have designed an approximate, multidimensional generalized Riemann problem (GRP) solver. The multidimensional Riemann solver takes the four states that come together at an edge as input states and provides the resolved state (traditionally called a strongly-interacting state) and multidimensional fluxes as output. The output can then be used to extend the strongly-interacting state and its fluxes in time. The edge-based arrangement of electric and magnetic fields for CED in Fig. 1 shows that the multidimensional GRP solver provides exactly the desired edge-based data at the very location this data is needed. This highlights the special utility of the multidimensional GRP solver for CED and other involution-constrained applications. In this paper, we have designed such an approximate, multidimensional GRP solver for linear hyperbolic systems with stiff, linear source terms. As a result, a one-step update that is temporally second order accurate is achieved.

Our formulation produces an overall constraint-preserving time-stepping strategy based on the GRP that is provably L-stable in the presence of stiff source terms. Our multidimensional GRP formulation, while specialized for CED, is generally applicable to any linear hyperbolic system with stiff, linear source terms.

The multidimensional GRP presented here is intended to be a building block for low dispersion, low dissipation higher order schemes for CED. It could also find utility in aeroacoustics. We also recognize that multidimensional Riemann solvers have found great utility as nodal solvers in Arbitrary Lagrangian Eulerian (ALE) schemes [68, 69]. The availability of multidimensional GRP solvers is expected to greatly simplify the design of higher order ALE schemes because the GRP provides a more accurate trajectory of the strongly-interacting state at each node. Likewise, the Taylor series-based schemes that result from the multidimensional GRP indeed reduce the number of reconstruction stages in ALE schemes. In subsequent papers we will pursue such innovations as well as further develop the field of CED.

Acknowledgements Arijit Hazra acknowledges support from the Airbus chair on Mathematics of Complex Systems at TIFR-CAM to visit University of Notre Dame. Several simulations were performed on a cluster at UND that is run by the Center for Research Computing. Computer support on NSF's XSEDE and Blue Waters computing resources is also acknowledged.

Funding Dinshaw S. Balsara acknowledges support via NSF Grants NSF-ACI-1533850, NSF-DMS-1622457, NSF-ACI-1713765 and NSF-DMS-1821242. Arijit Hazra would like to acknowledge funding support from the Ramanujan Fellowship (RJF/2022/000046) administered by SERB-DST, India.

Data Availability The corresponding author will make numerically simulated data available under reasonable request.

Declarations

Conflict of interest There is no conflict of interest to declare.

References

1. Yee, K.: Numerical solution of initial boundary value problems involving Maxwell's equations in isotropic media. IEEE Trans. Antennas Propag. **14**(3), 302–307 (1966)
2. Taflove, A., Brodwin, M.E.: Numerical solution of steady-state electromagnetic scattering problems using the time-dependent Maxwell's equations. IEEE Trans. Microw. Theory Tech. **23**(8), 623–630 (1975)
3. Taflove, A.: Review of the formulation and applications of the finite-difference time-domain method for numerical modeling of electromagnetic wave interactions with arbitrary structures. Wave Motion **10**(6), 547–582 (1988)
4. Taflove, A., Hagness, S.C.: Computational Electrodynamics, vol. 28. Artech House Publishers, Norwood (2000)
5. Taflove, A., Hagness, S.C.: Finite-difference time-domain solution of Maxwell's equations. Wiley Encyclopedia of Electrical and Electronics Engineering, pp. 1–33 (1999)
6. Angulo, L., Alvarez, J., Pantoja, M., Garcia, S., Bretones, A.: Discontinuous Galerkin time domain methods in computational electrodynamics: state of the art. In: Forum for Electromagnetic Research Methods and Application Technologies, vol. 10, pp. 1–24 (2015)
7. Hesthaven, J.S., Warburton, T.: Nodal high-order methods on unstructured grids: I. Time-domain solution of Maxwell's equations. J. Comput. Phys. **181**(1), 186–221 (2002)
8. Hesthaven, J.S., Warburton, T.: Nodal Discontinuous Galerkin Methods: Algorithms, Analysis, and Applications. Springer, Berlin (2007)
9. Chen, J., Liu, Q.H.: Discontinuous Galerkin time-domain methods for multiscale electromagnetic simulations: A review. Proc. IEEE **101**(2), 242–254 (2012)
10. Chen, J., Liu, Q.H.: A non-spurious vector spectral element method for Maxwell's equations. Prog. Electromagn. Res. **96**, 205–215 (2009)
11. Ren, Q., Tobón, L.E., Sun, Q., Liu, Q.H.: A new 3-D nonspurious discontinuous Galerkin spectral element time-domain (DG-SETD) method for Maxwell's equations. IEEE Trans. Antennas Propag. **63**(6), 2585–2594 (2015)
12. Wang, H., Xu, L., Li, B., Descombes, S., Lantéri, S.: A new family of exponential-based high-order DGTD methods for modeling 3-D transient multiscale electromagnetic problems. IEEE Trans. Antennas Propag. **65**(11), 5960–5974 (2017)
13. Sun, Q., Zhang, R., Zhan, Q., Liu, Q.H.: A novel coupling algorithm for perfectly matched layer with wave equation-based discontinuous Galerkin time-domain method. IEEE Trans. Antennas Propag. **66**(1), 255–261 (2017)
14. Balsara, D.S., Amano, T., Garain, S., Kim, J.: A high-order relativistic two-fluid electrodynamic scheme with consistent reconstruction of electromagnetic fields and a multidimensional Riemann solver for electromagnetism. J. Comput. Phys. **318**, 169–200 (2016). https://doi.org/10.1016/j.jcp.2016.05.006
15. Balsara, D.S., Taflove, A., Garain, S., Montecinos, G.: Computational electrodynamics in material media with constraint-preservation, multidimensional Riemann solvers and sub-cell resolution—Part I, second-order FVTD schemes. J. Comput. Phys. **349**, 604–635 (2017). https://doi.org/10.1016/j.jcp.2017.07.024
16. Balsara, D.S., Garain, S., Taflove, A., Montecinos, G.: Computational electrodynamics in material media with constraint-preservation, multidimensional Riemann solvers and sub-cell resolution—Part II, higher order FVTD schemes. J. Comput. Phys. **354**, 613–645 (2018). https://doi.org/10.1016/j.jcp.2017.10.013
17. Balsara, D.S., Käppeli, R.: Von Neumann stability analysis of globally divergence-free RKDG schemes for the induction equation using multidimensional Riemann solvers. J. Comput. Phys. **336**, 104–127 (2017)
18. Balsara, D.S., Käppeli, R.: Von Neumann stability analysis of globally constraint-preserving DGTD and PNPM schemes for the Maxwell's equations using multidimensional Riemann solvers. J. Comput. Phys. **376**, 1108–1137 (2019)
19. Hazra, A., Chandrashekar, P., Balsara, D.S.: Globally constraint-preserving FR/DG scheme for Maxwell's equations at all orders. J. Comput. Phys. **394**, 298–328 (2019). https://doi.org/10.1016/j.jcp.2019.06.003
20. Balsara, D.S.: Divergence-free adaptive mesh refinement for magnetohydrodynamics. J. Comput. Phys. **174**(2), 614–648 (2001). https://doi.org/10.1006/jcph.2001.6917
21. Balsara, D.S.: Second-order-accurate schemes for magnetohydrodynamics with divergence-free reconstruction. Astrophys. J. Suppl. Ser. **151**(1), 149 (2004)
22. Balsara, D.S.: Divergence-free reconstruction of magnetic fields and WENO schemes for magnetohydrodynamics. J. Comput. Phys. **228**(14), 5040–5056 (2009)
23. Balsara, D.S., Dumbser, M.: Divergence-free MHD on unstructured meshes using high order finite volume schemes based on multidimensional Riemann solvers. J. Comput. Phys. **299**, 687–715 (2015). https://doi.org/10.1016/j.jcp.2015.07.012

24. Xu, Z., Balsara, D.S., Du, H.: Divergence-free WENO reconstruction-based finite volume scheme for solving ideal MHD equations on triangular meshes. Commun. Comput. Phys. **19**(4), 841–880 (2016). https://doi.org/10.4208/cicp.050814.040915a
25. Balsara, D.S.: Multidimensional HLLE Riemann solver: application to Euler and magnetohydrodynamic flows. J. Comput. Phys. **229**(6), 1970–1993 (2010). https://doi.org/10.1016/j.jcp.2009.11.018
26. Balsara, D.S.: A two-dimensional HLLC Riemann solver for conservation laws: application to Euler and magnetohydrodynamic flows. J. Comput. Phys. **231**(22), 7476–7503 (2012). https://doi.org/10.1016/j.jcp.2011.12.025
27. Balsara, D.S.: Multidimensional Riemann problem with self-similar internal structure. Part I—application to hyperbolic conservation laws on structured meshes. J. Comput. Phys. **277**, 163–200 (2014). https://doi.org/10.1016/j.jcp.2014.07.053
28. Balsara, D.S.: Three dimensional HLL Riemann solver for conservation laws on structured meshes; application to Euler and magnetohydrodynamic flows. J. Comput. Phys. **295**, 1–23 (2015)
29. Balsara, D.S., Dumbser, M., Abgrall, R.: Multidimensional HLLC Riemann solver for unstructured meshes-with application to Euler and MHD flows. J. Comput. Phys. **261**, 172–208 (2014)
30. Balsara, D.S., Dumbser, M.: Multidimensional Riemann problem with self-similar internal structure. Part II—application to hyperbolic conservation laws on unstructured meshes. J. Comput. Phys. **287**, 269–292 (2015). https://doi.org/10.1016/j.jcp.2014.11.004
31. Balsara, D.S., Vides, J., Gurski, K., Nkonga, B., Dumbser, M., Garain, S., Audit, E.: A two-dimensional Riemann solver with self-similar sub-structure-alternative formulation based on least squares projection. J. Comput. Phys. **304**, 138–161 (2016)
32. Balsara, D.S., Nkonga, B.: Multidimensional Riemann problem with self-similar internal structure-Part III-a multidimensional analogue of the HLLI Riemann solver for conservative hyperbolic systems. J. Comput. Phys. **346**, 25–48 (2017)
33. Smith, W.S., Razmadze, A., Shao, X.M., Drewniak, J.L.: A hierarchy of explicit low-dispersion FDTD methods for electrically large problems. IEEE Trans. Antennas Propag. **60**(12), 5787–5800 (2012). https://doi.org/10.1109/TAP.2012.2209860
34. Williamson, J.: Low-storage Runge–Kutta schemes. J. Comput. Phys. **35**(1), 48–56 (1980). https://doi.org/10.1016/0021-9991(80)90033-9
35. Hu, F., Hussaini, M., Manthey, J.: Low-dissipation and low-dispersion Runge–Kutta schemes for computational acoustics. J. Comput. Phys. **124**(1), 177–191 (1996). https://doi.org/10.1006/jcph.1996.0052
36. Berland, J., Bogey, C., Marsden, O., Bailly, C.: High-order, low dispersive and low dissipative explicit schemes for multiple-scale and boundary problems. J. Comput. Phys. **224**(2), 637–662 (2007). https://doi.org/10.1016/j.jcp.2006.10.017
37. Niegemann, J., Diehl, R., Busch, K.: Efficient low-storage Runge–Kutta schemes with optimized stability regions. J. Comput. Phys. **231**(2), 364–372 (2012). https://doi.org/10.1016/j.jcp.2011.09.003
38. Diehl, R., Busch, K., Niegemann, J.: Comparison of low-storage Runge–Kutta schemes for discontinuous Galerkin time-domain simulations of Maxwell's equations. J. Comput. Theor. Nanosci. **7**(8), 1572–1580 (2010)
39. Sármány, D., Botchev, M.A., van der Vegt, J.J.W.: Dispersion and dissipation error in high-order Runge–Kutta discontinuous Galerkin discretisations of the Maxwell's equations. J. Sci. Comput. **33**(1), 47–74 (2007). https://doi.org/10.1007/s10915-007-9143-y
40. Chen, M.H., Cockburn, B., Reitich, F.: High-order RKDG methods for computational electromagnetics. J. Sci. Comput. **22–23**(1–3), 205–226 (2005). https://doi.org/10.1007/s10915-004-4152-6
41. Dumbser, M., Balsara, D.S., Toro, E.F., Munz, C.D.: A unified framework for the construction of one-step finite volume and discontinuous Galerkin schemes on unstructured meshes. J. Comput. Phys. **227**(18), 8209–8253 (2008). https://doi.org/10.1016/j.jcp.2008.05.025
42. Dumbser, M., Zanotti, O., Hidalgo, A., Balsara, D.S.: ADER-WENO finite volume schemes with space-time adaptive mesh refinement. J. Comput. Phys. **248**, 257–286 (2013). https://doi.org/10.1016/j.jcp.2013.04.017
43. Balsara, D.S., Rumpf, T., Dumbser, M., Munz, C.D.: Efficient, high accuracy ADER-WENO schemes for hydrodynamics and divergence-free magnetohydrodynamics. J. Comput. Phys. **228**(7), 2480–2516 (2009). https://doi.org/10.1016/j.jcp.2008.12.003
44. Balsara, D.S., Meyer, C., Dumbser, M., Du, H., Xu, Z.: Efficient implementation of ADER schemes for Euler and magnetohydrodynamical flows on structured meshes—speed comparisons with Runge–Kutta methods. J. Comput. Phys. **235**, 934–969 (2013). https://doi.org/10.1016/j.jcp.2012.04.051
45. Taube, A., Dumbser, M., Munz, C.D., Schneider, R.: A high-order discontinuous Galerkin method with time-accurate local time stepping for the Maxwell equations. Int. J. Numer. Model. Electron. Networks Devices Fields **22**(1), 77–103 (2009). https://doi.org/10.1002/jnm.700

46. Floch, P.L., Raviart, P.A.: An asymptotic expansion for the solution of the generalized Riemann problem Part I: general theory. Annales de l'Institut Henri Poincaré C, Analyse non linéaire **5**, 179–207 (1988). https://doi.org/10.1016/S0294-1449(16)30350-X
47. Titarev, V.A., Toro, E.F.: ADER: Arbitrary high order Godunov approach. J. Sci. Comput. **17**(1), 609–618 (2002)
48. Titarev, V.A., Toro, E.F.: ADER schemes for three-dimensional non-linear hyperbolic systems. J. Comput. Phys. **204**(2), 715–736 (2005)
49. Toro, E.F., Millington, R., Nejad, L.: Towards very high order Godunov schemes. In: Godunov methods, pp. 907–940. Springer, Berlin (2001)
50. Toro, E.F., Titarev, V.A.: Solution of the generalized Riemann problem for advection-reaction equations. Proc. Math. Phys. Eng. Sci. **458**(2018), 271–281 (2002)
51. Qian, J., Li, J., Wang, S.: The generalized Riemann problems for compressible fluid flows: towards high order. J. Comput. Phys. **259**, 358–389 (2014). https://doi.org/10.1016/j.jcp.2013.12.002
52. Montecinos, G.I., Toro, E.F.: Reformulations for general advection–diffusion–reaction equations and locally implicit ADER schemes. J. Comput. Phys. **275**, 415–442 (2014)
53. Wu, K., Yang, Z., Tang, H.: A third-order accurate direct Eulerian GRP scheme for the Euler equations in gas dynamics. J. Comput. Phys. **264**, 177–208 (2014)
54. Goetz, C.R., Dumbser, M.: A novel solver for the generalized Riemann problem based on a simplified LeFloch-Raviart expansion and a local space-time discontinuous Galerkin formulation. J. Sci. Comput. **69**(2), 805–840 (2016)
55. Goetz, C.R., Balsara, D.S., Dumbser, M.: A family of HLL-type solvers for the generalized Riemann problem. Comput. Fluids **169**, 201–212 (2018). https://doi.org/10.1016/j.compfluid.2017.10.028
56. Ben-Artzi, M., Falcovitz, J.: A second-order Godunov-type scheme for compressible fluid dynamics. J. Comput. Phys. **55**(1), 1–32 (1984)
57. Ben-Artzi, M., Falcovitz, J.: An upwind second-order scheme for compressible duct flows. SIAM J. Sci. Stat. Comput. **7**(3), 744–768 (1986)
58. Ben-Artzi, M., Falcovitz, J.: Generalized Riemann Problems in Computational Fluid Dynamics, vol. 11. Cambridge University Press, Cambridge (2003)
59. Ben-Artzi, M.: The generalized Riemann problem for reactive flows. J. Comput. Phys. **81**(1), 70–101 (1989)
60. Ben-Artzi, M., Birman, A.: Computation of reactive duct flows in external fields. J. Comput. Phys. **86**(1), 225–255 (1990)
61. Bourgeade, A., Floch, P.L., Raviart, P.A.: An asymptotic expansion for the solution of the generalized Riemann problem. Part 2: application to the equations of gas dynamics. Annales de l'Institut Henri Poincaré C, Analyse non linéaire **6**, 437–480 (1989). https://doi.org/10.1016/S0294-1449(16)30310-9
62. Balsara, D.S., Li, J., Montecinos, G.I.: An efficient, second order accurate, universal generalized Riemann problem solver based on the HLLI Riemann solver. J. Comput. Phys. **375**, 1238–1269 (2018). https://doi.org/10.1016/j.jcp.2018.09.018
63. Balsara, D.S., Dumbser, M., Abgrall, R.: Multidimensional HLLC Riemann solver for unstructured meshes—with application to Euler and MHD flows. J. Comput. Phys. **261**, 172–208 (2014). https://doi.org/10.1016/j.jcp.2013.12.029
64. J, Li., Z, Du.: A two-stage fourth order time-accurate discretization for Lax–Wendroff type flow solvers I. Hyperbolic conservation laws. SIAM J. Sci. Comput. **38**(5), A3046–A3069 (2016). https://doi.org/10.1137/15M1052512
65. Christlieb, A.J., Gottlieb, S., Grant, Z., Seal, D.C.: Explicit strong stability preserving multistage two-derivative time-stepping schemes. J. Sci. Comput. **68**(3), 914–942 (2016). https://doi.org/10.1007/s10915-016-0164-2
66. Grant, Z., Gottlieb, S., Seal, D.C.: A strong stability preserving analysis for explicit multistage two-derivative time-stepping schemes based on Taylor series conditions. Commun. Appl. Math. Comput. **1**(1), 21–59 (2019). https://doi.org/10.1007/s42967-019-0001-3
67. Harten, A., Lax, P.D., Leer, B.V.: On upstream differencing and Godunov-type schemes for hyperbolic conservation laws. SIAM Rev. **25**(1), 35–61 (1983)
68. Boscheri, W., Dumbser, M., Balsara, D.S.: High-order ADER-WENO ALE schemes on unstructured triangular meshes-application of several node solvers to hydrodynamics and magnetohydrodynamics. Int. J. Numer. Methods Fluids **76**(10), 737–778 (2014). https://doi.org/10.1002/fld.3947
69. Boscheri, W., Balsara, D.S., Dumbser, M.: Lagrangian ADER-WENO finite volume schemes on unstructured triangular meshes based on genuinely multidimensional HLL Riemann solvers. J. Comput. Phys. **267**, 112–138 (2014). https://doi.org/10.1016/j.jcp.2014.02.023